Temporal Variations in Hotspot Volcanic Production Related to Interactions Between Upwelling Mantle Plumes and Phase Transitions

A Thesis

Presented in Partial Fulfillment of the Requirements for the

Degree of Master of Science

with a

Major in Geology

in the

College of Graduate Studies

University of Idaho

by

Derek J. Neuharth

Major Professor: Eric L. Mittelstaedt, Ph.D.

Committee Members: Jerry P. Fairley, Ph.D.; John B. Naliboff, Ph.D.

Department Administrator: Leslie L. Baker, Ph.D.

August 2018

Authorization To Submit Thesis

The thesis of Derek J. Neuharth, submitted for the degree of Master of Science with a major in Geology and titled, “Temporal Variations in Hotspot Volcanic Production Related to Interactions Between Upwelling Mantle Plumes and Phase Transitions,” has been reviewed in final form. Permission, as indicated by the signatures and dates given below, is now granted to submit final copies to the College of Graduate Studies for approval.

Major Professor: _____ Date: _____
Eric L. Mittelstaedt, Ph.D.

Committee Members: _____ Date: _____
Jerry P. Fairley, Ph.D.

_____ Date: _____
John B. Naliboff, Ph.D.

Department

Administrator: _____ Date: _____
Leslie L. Baker, Ph.D.

Abstract

Observations at numerous hotspots around the globe, such as Hawaii and Louisville, find periodic variations in volcanic production with time. For example, the volcanic production rate along the Hawaiian seamount chain varies from 0.05 to 0.25 $km^3\ yr^{-1}$ at periods of ~15 Myr, while volcanic production rate along the Louisville seamount chain in the southern Pacific Ocean has consistently declined over the past ~40 Myr. One possible explanation for these variations is long-term interaction of upwelling mantle plumes with mantle phase transitions. While previous studies carefully quantify the initial interaction and subsequent penetration or inhibition of a plume as it encounters the 660 km phase boundary and traverses the transition zone, the long term interaction of plume upwelling and phase boundaries in the mantle is not well constrained. To assess the impact of plume-phase transition interaction on observed variability in hotspot volcanic output, I use the Advanced Solver for Problems in Earth's ConvecTion (ASPECT) code to numerically simulate upwelling of an isolated plume under the Anelastic Liquid Approximation (ALA). I use a 2D annulus geometry with a 90° opening width and mantle thickness of 2855 km. Plume upwelling is initiated by imposing anomalously warm (ΔT 550 K) temperatures across a zone 600 km wide centered at the base of the model. At the 660 km and 410 km depth mantle phase transitions I simulate changes in density, viscosity, and the release of latent heat. Models evolve for up to 400 Myr. To test the effect of differing mantle compositions, I vary the Clapeyron slopes from 0 to 4 MPa and -4 to 0 MPa at the 410 km and 660 km phase transitions, respectively. Similar to other studies, results show an initial flattening of the plume head at the 660 km transition before penetration and subsequent acceleration across the 410 km transition, coinciding with mild flattening of the 660 km, and deepening of the 410 km. At sufficiently low 660 km transition Clapeyron slopes (~-3.2 MPa K^{-1}), secondary plumes form at a mid-mantle thermal boundary layer that forms as inhibited material spreads laterally underneath the transition. The spacing of these secondary plumes (~200-1200 km) is similar to surface observations (e.g., Iceland, East African Rift). By including imposed surface velocities (0-8 cm yr^{-1}), volume flux variations are seen from plume conduit instabilities that form when the conduit tilts ~88º from vertical. These variations have a periodicity between ~4.1-37.9 Myr, which is similar to those seen at Hawaii and Iceland.

Acknowledgements

I would like to sincerely thank Eric Mittelstaedt for all the help and guidance he's given me, as well as for the opportunity to work at the University of Idaho. I would also like to thank my committee members, Jerry Fairley and John Naliboff for helping with any problems I ran in to during this project. Lastly, I would like to thank Thomas Morrow for answering any random questions I had throughout the past two years, and the National Science Foundation for funding this project.

Table of Contents

List of Tables

List of Figures

1. Introduction

Multiple hotspots around the globe exhibit variable volcanic production. From a list of 69 hotspots, at least 13 have long-lived (>50 Myr) age-progressive volcanism (*Ito and van Keken,* 2007), consistent with the standard model of mantle plume-derived volcanism (e.g., *Morgan*, 1971). Of these 13 hotspots, seismic imaging identifies low-velocity, columnar structures below several of them (*Zhao,* 2004; *Montelli et al*., 2006; *Wolfe et al.,* 2009*; French and Romanowicz,* 2015), suggesting a deep mantle plume source. Contrary to expectations of steady upwelling in a plume stem (e.g., *Coffin et al., 2002*), magmatic output along age-progressive hotspot volcanic chains can vary by more than an order of magnitude (e.g., *Wessel*, 2016). For example, estimates of magmatic output from the Louisville hotspot, located in the southern Pacific Ocean, are relatively constant before gradually decreasing after ~40 Ma (*Beier et al*., 2011). In contrast, volcanic output from the Hawaiian and Iceland hotspots varies regularly within periods of millions of years (*Vidal and Bonneville*, 2004; *O'Connor et al*., 2001; *Wessel*, 2016). The causes for different modes of volcanic production between hotspots (e.g., Hawaii, Iceland, and Louisville) is not well understood, and in some cases, may be linked to deep mantle processes that perturb plume upwelling.

Periodic variations in volcanic production along the Hawaiian hotspot are relatively well characterized (*Van Ark and Lin*, 2004; *Vidal and Bonneville*, 2004; *Wessel*, 2016). These studies estimate that the volcanic production varies from 0.05 to 0.25 $km^3\ yr^{-1}$ with time between peaks in production ranging from ~5 to 30.8 Myr. Such variations in volcanic production may be caused by instabilities in the plume conduit associated with a tilted plume, or by the propagation of solitary waves through a plume conduit (*Vidal and Bonneville*, 2004).

Icelandic lavas show isotopic variation with volume flux, with higher radiogenic Pb isotopes found at magmatic production peaks (18.171 to 19.084 for $^{206}Pb/^{204}Pb$; *Hanan and Schilling*, 1997). At Iceland, variations in magmatic production, possibly caused by variability in plume production, have a periodicity between ~5-10 Myr and may be responsible for the formation of V-shaped ridges along the Reykjanes Spreading Ridge (*O'Connor et al*., 2001; *Ito*, 2001). Rift propagation is a mechanism proposed to have formed the V-shaped ridges that may not require variation in plume production; however, neither the simple thermal or rift propagation models can fully explain observations in the region, and a hybrid of the two is likely (*Hey et al*., 2010; *Hey et al*., 2016). Recently, it has been proposed that gradients in mantle properties (water content, temperature, and composition) may propagate buoyant mantle upwellings southward from Iceland, where the upwellings density structure may

cause the observed variations in magma production (*Martinez and Hey*, 2017). Seismic imaging of the Iceland hotspot suggests a south-eastern tilt and connection between it and the nearby south-eastern tilting Jan-Mayen plume near the mantle transition zone, although isotopically they are distinct (*Rickers et al*., 2013).

Volcanism from the Louisville hotspot has continued for ~80 Myr, creating a ~4300 km long seamount chain (*Vanderkluysen et al.,* 2014). Volcanic production along the Louisville chain was approximately constant until 45 Ma when it briefly increased as the plume interacted with the Wishbone Scarp fracture zone. Since 40 Ma, volcanic production has steadily declined (*Beier et al*., 2011). Unlike Hawaii and Iceland, there is no evidence for periodic increases in volcanic production and erupted lavas show little geochemical variation, with nearly uniform radiogenic isotope ratios (*Vanderkluysen et al*., 2014; *Beier et al*., 2011).

1.1 Mantle convection and Plume Dynamics

Convection in Earth's mantle is similar to Rayleigh-Benard convection, where a fluid heated from below and cooled from above develops convective instabilities when the Rayleigh number (Ra), a dimensionless number showing whether heat is transferred primarily through conduction or convection, exceeds a critical value. Growth of convective instabilities includes formation of cold downwellings and warm upwellings. In the mantle, downwellings take the form of subducting oceanic lithosphere beneath convergent plate boundaries. Subducted lithosphere descends deep into the mantle, and in some cases, may reach the core-mantle boundary (CMB; *van der Hilst et al*., 1997; *Zhao et al*., 2013). Upwellings in the Earth's mantle form divergent plate margins where passive upwelling leads to partial melting and consequent volcanism along the mid-ocean ridge. Additionally, upwellings take the form of buoyantly rising columns of mantle rock (i.e., a mantle plume) that partially melt near the surface causing eruptions along hotspot volcanic seamount chains (*Schubert et al*., 2001).

Mantle plumes are commonly defined as localized upwellings that rise from the CMB due to instabilities in the thermal boundary layer (TBL) overlying the core (*Schubert et al*., 2001). Given a near constant supply of material from the TBL and no external disturbances, plumes are expected to form an axisymmetric, steady conduit (e.g., *Albers and Christensen*, 1996). However, several potential factors can perturb the plume and cause variability in the conduit, including compositionally variable material introducing buoyancy differences within a

rising plume stem, solitary waves generated in the plume source region (*Schubert and Olson*, 1989; *Olson*, 1990), and plate-motion induced tilting of the plume conduit in the upper mantle (*Whitehead*, 1982).

Of particular interest here is the development of instabilities in tilted plume conduits. Numerical and laboratory experiments find that increasing conduit tilt decreases along-conduit plume velocity and increases plume radius. An increase in the radius of a tilted plume increases the component of buoyancy oblique to the conduit, promoting formation of an instability in the plume conduit and a consequent vertical pulse of material when the conduit tilts >~60 degrees from vertical [*Whitehead*, 1982]. Although *Whitehead's* [1982] experiments demonstrate formation of individual diapirs from a plume conduit, the physical experiments used fluids of different inherent densities, not thermally induced upwelling such as expected within the mantle. The neglect of thermal diffusion on conduit stability has led others to question whether these instabilities can occur under mantle conditions (*Kerr et al*., 2008; *Meriaux et al*., 2011). Indeed, thermal diffusivity has a stabilizing effect when the Ra of the plume conduit relative to the surrounding mantle (Ra_{pc}) is less than 300. Using values appropriate to the Earth's mantle, *Kerr et al.* (2008) estimated Ra_{pc} for tilted plume conduits to be between 54 and 104 in the upper mantle, suggesting that even horizontal conduits will remain stable. Recently, *Meriaux et al.* [2011] suggested that upper mantle Ra_{pc} values may be larger, but that instability growth timescales are greater than the time for plume material to traverse the upper mantle, which indicates that tilted plumes should remain stable in the upper mantle. However, these studies did not account for compressibility, phase changes, or the depth-dependence of viscosity, thermal conductivity, and thermal expansion.

1.2 Mantle transition zone

Increasing pressure and temperature with depth in the mantle cause olivine to undergo several phase transitions. Of the known phase transitions in the mantle, three of the most significant for mantle dynamics result in olivine transitioning into a denser phase. These phase transitions occur between ~410 km and ~660 km depth, a region known as the mantle transition zone (*Flanagan and Shearer*, 1998). In order of increasing depth, the transitions are Olivine to Wadsleyite (~410 km), an exothermic reaction with a Clapeyron slope between 1 and 4 MPa K^{-1} (*Akaogi et al*., 1989; *Katsura et al.,* 2004), Wadsleyite to Ringwoodite (~520 km), an exothermic reaction with a Clapeyron slope between 2.8 and 7 MPa K^{-1} (*Yu et al*., 2008; *Suzuki et al*., 2000), and Ringwoodite to Bridgmanite and Ferropericlase (~660 km), an

endothermic reaction with a Clapeyron slope between -4 and -0.4 MPa K^{-1} (*Ghosh et al*., 2013; *Ito et al.*, 1990; *Faccenda & Zilio*, 2017).

The Clapeyron slope is the slope of the curve in pressure-temperature space where two phases are in equilibrium (*Turcotte and Schubert*, 2014). Local changes to the magnitude of the Clapeyron slope may have important consequences for mantle dynamics. For example, a positive Clapeyron slope (exothermic reaction) will be locally elevated when exposed to a cold subducting slab, causing the slab to transition to the denser phase at a shallower depth than the surrounding mantle, promoting downwelling. A positive Clapeyron slope will be locally deepened in the presence of higher temperatures within a mantle plume, causing the plume material to transition to a less dense phase at a deeper depth than the surrounding mantle, promoting upwelling. In contrast, a negative Clapeyron slope indicates an endothermic reaction, which will deepen within a subducting slab and elevate within a mantle plume, inhibiting downward motion of slabs and upward motion of plumes (e.g., *Schubert*, 1975; Figure 1.1).

Seismic evidence suggests that in most places mantle plumes and subducted lithosphere travel through the entirety of the mantle. However, in some locations mantle plumes pond under the transition zone (*Zhao*, 2007) and subducting slabs deflect at the 660 km transition (*Fukao and Obayashi*, 2013). Thus, some amount of layering may occur intermittently in the mantle (*Tackley*, 2008). Recently, it has been suggested that layering is likely dependent on the Ra, with phase transition Clapeyron slopes being temporally variable, making the role of the 410 and 660 km phase transitions areas of intense interest for understanding mantle dynamics (*Stixrude et al*., 2016).

Multiple studies have found that, with sufficiently negative Clapeyron slopes (~-4 MPa K^{-1}), plumes are completely inhibited at the 660 km phase transition (*Nakakuki et al*., 1994; *Schubert et al*., 1995). In some case, inhibition at the discontinuity results in a TBL where secondary plumes can initiate (*Brunet et al*., 2000). Recently, using numerical simulations of a compressible mantle to examine the effects of different Clapeyron slopes at the 660 km transition, *Bossmann and Van Keken* [2013] found three types of plume-phase transition interaction. For whole mantle Ra > $3x10^6$, plumes can penetrate the phase transition at the plume center (>-2.75 MPa K^{-1}), penetrate away from symmetry axis forming a ring structure (-2.75 to -2.95 MPa K^{-1}), or, cease to rise and spread beneath the 660 km phase transition below a critical Clapeyron slope (<-2.95 MPa K^{-1}). However, their models only simulate

plume-phase transition interactions for ~15 Myr, much shorter than the lifespan of hotspots associated with mantle plumes (*Ito and van Keken*, 2007).

To examine how the 410 km and 660 km phase transitions affect long-term plume dynamics, I use numerical simulations of a single, whole mantle plume with both phase transitions and surface plate motions. I vary the Clapeyron slopes of these phase changes across the range of existing experimental values to test whether long-term interactions between a plume and phase transitions may be responsible for variable volcanic production seen at hotspots such as Hawaii and Iceland. Results indicate that the 660 km transition is important in the formation of a mid-mantle TBL. At sufficiently low 660 Clapeyron slopes (<-3.2 MPa K^{-1}), plume material ponds, resulting in the formation of secondary plumes. The timing and lifespan of secondary plumes are related to the magnitude of the 660 km Clapeyron slope. Variable plume volume flux is observed when including plate motion, and generally results from instabilities formed as a plume conduit tilts. The effect of different Clapeyron slopes at phase transitions on the periodicity of plate-motion-driven variability is minor.

2. Methods

2.1 Governing Equations

I perform numerical simulations of a plume rising through a compressible mantle with mid-mantle phase transitions using a custom material model within the Advanced Solver for Earth's ConvecTion code (ASPECT 2.0.0-pre; deal.II 8.5.0) (e.g*., Kronbichler et al.,* 2012*; Heister et al*. 2017). Using the Anelastic Liquid Approximation (ALA) (e.g., *Jarvis and McKenzie*, 1980; *King et al*., 2010), ASPECT solves the equations of conservation of mass, momentum and energy,

$$\nabla \cdot (\bar{\rho}\mathbf{u}) = 0, \tag{1}$$

$$-\nabla \cdot \left[2\eta \left(\varepsilon(\mathbf{u}) - \frac{1}{3}(\nabla \cdot \mathbf{u})\mathbf{1}\right)\right] + \nabla \mathrm{P}' = \left(\frac{\partial \rho(\bar{P},\bar{\mathrm{T}})}{\partial \mathrm{p}}\mathrm{P}' + \frac{\partial \rho(\bar{P},\bar{\mathrm{T}})}{\partial \mathrm{T}}\mathrm{T}'\right)\mathbf{g}, \tag{2}$$

$$\bar{\rho}\mathrm{Cp}\left(\frac{\partial \mathrm{T}}{\partial \mathrm{t}} + \mathrm{u} \cdot \nabla \mathrm{T}\right) - \nabla \cdot \mathrm{k}\nabla \mathrm{T} = 2\eta \left(\varepsilon(\mathbf{u}) - \frac{1}{3}(\nabla \cdot \mathbf{u})\mathbf{1}\right) : \left(\varepsilon(\mathbf{u}) - \frac{1}{3}(\nabla \cdot \mathbf{u})\mathbf{1}\right) \tag{3}$$

$$+ \alpha\bar{\rho}\mathrm{T}\,(\mathbf{u} \cdot \mathbf{g})$$

$$+ \rho \mathrm{T}\,\Delta \mathrm{S}\left(\frac{\partial\,\Gamma}{\partial \mathrm{t}}\,\mathbf{u} \cdot \nabla\Gamma\right),$$

where ρ is density, $\boldsymbol{u}$ is velocity (bold characters indicate vectors), η is viscosity, T is temperature, P is pressure, $\boldsymbol{g}$ is gravity, Cp is specific heat capacity, k is thermal conductivity, α is thermal expansivity, and $\boldsymbol{\varepsilon(u)}$ is the strain rate tensor (an overbar indicates the reference profile for the given variable). This formulation of the conservation of momentum (Equation 2) assumes that changes in momentum are driven by small variations in density caused by temperature and pressure deviations from their reference states. Conservation of energy (Equation 3) includes right hand side heat source terms that account for (from left to right) viscous dissipation, adiabatic heating, and latent heat release at phase boundaries. Latent heat release at phase boundaries is determined by the change in entropy, ΔS, of the reaction, and the fraction of material, Γ, that has undergone the phase change. Values for reference parameters are given in table 2.1.

2.2 Phase function

Phase transitions within this model are based on pressure and temperature deviations from chosen initial transition values. I define the fraction of material, Γ, that has

undergone a phase change using a hyperbolic phase function (e.g., *Christensen and Yuen*, 1985),

$$\Gamma = \frac{1}{2}\left(1 + \tanh\left(\frac{\mathrm{P}_d}{P_w}\right)\right), \tag{4}$$

$$\mathrm{P}_d = \mathrm{P} - \mathrm{P}_t - \gamma(\mathrm{T} - \mathrm{T}_t), \tag{5}$$

where P_d is the pressure deviation associated with differences in dynamic pressure and mantle temperature relative to the model reference state, P_w is the pressure change over a specified transition width, γ is the Clapeyron slope, and P_t and T_t are the pressure and temperature of the transition, respectively. Viscosity, thermal expansivity, and thermal conductivity have phase dependent parameters that I do not change gradationally; I assume that these parameters change when Γ equals 0.5 (e.g. *Dannberg et al*., 2017; Table 2.2).

2.3 Reference Profiles

In this study, I define density under the ALA as a pressure, temperature, and phase dependent function that varies based on deviations in temperature and pressure from reference profiles (Figure 2.1 and 2.2),

$$\rho = \bar{\rho}(1 - \alpha \mathrm{T}_{dev} + \mathrm{KP}_{dev}) + \sum \rho_{jump,i}\, \Gamma_i, \tag{6}$$

where $\bar{\rho}$ is the reference density profile, α is thermal expansivity, K is mantle compressibility, P_{dev} and T_{dev} are deviations in pressure and temperature from the refence profiles, ρ_{jump} is the phase associated density jump, and Γ_i is the fraction of material that has undergone phase change i (= 410 km transition or 660 km transition). Reference profiles for density, temperature, and pressure are defined using a function dependent on the normalized depth derived from the Adams-Williamson equation of state (*King et al*., 2010),

$$\bar{\rho} = \rho_{ref} \exp\left(\frac{Di\, z}{Gr}\right), \tag{7}$$

$$\overline{\mathrm{T}} = \mathrm{T}_{ref} \exp\left(\frac{Di\, z}{Gr}\right) + \sum \mathrm{T}_{jump,i}\, \Gamma_i, \tag{8}$$

$$\overline{\mathrm{P}} = \int \left(\bar{\rho} + \sum \rho_{jump,i}\, \Gamma_i\right) \mathbf{g}\, \mathrm{dz}, \tag{9}$$

where $\bar{T}$ is the reference temperature profile, $\bar{P}$ is the reference pressure profile, T_{ref} is reference surface temperature, ρ_{ref} is reference density, z is dimensionless depth (scaled by the full height of the domain), and T_{jump} is the phase associated temperature jump. Although

the reference density profile does not include density jumps due to phase changes as does the full density, I include the effect of different densities in the reference pressure profile. *Di* and *Gr* represent the dissipation number and Grunheisen parameter defined as,

$$\mathrm{Di} = \frac{\alpha_r \mathbf{g} \mathrm{h}}{Cp}, \tag{10}$$

$$\mathrm{Gr} = \frac{\alpha_r}{(\mathrm{K}\rho_{ref}\mathrm{Cp})}, \tag{11}$$

where h is mantle thickness, α_r is the reference thermal expansivity, and Cp is specific heat. Temperature jumps at phase boundaries are dependent on the entropy change associated with the given phase change

$$\mathrm{T}_{jump} = \frac{\Delta \mathrm{S} \mathrm{T}_b}{Cp}, \tag{12}$$

$$\Delta \mathrm{S} = \frac{\gamma \rho_{jump}}{\rho_{ref}^2}, \tag{13}$$

where T_b and γ are the temperature and Clapeyron slope associated with the phase transition. Thermal expansivity and conductivity are pressure, temperature, and phase dependent and are defined as,

$$\alpha = (\mathrm{a}_0 + \mathrm{a}_1 \mathrm{T} + \mathrm{a}_2 \mathrm{T}^{-2}) \exp(-\mathrm{a}_3 \mathrm{P}), \tag{14}$$

$$\mathrm{k} = (\mathrm{c}_0 + \mathrm{c}_1 \mathrm{P}) \left(\frac{300}{T}\right)^{c_2}, \tag{15}$$

where a_i and c_i are phase dependent coefficients determined by inversion of experimental data (*Tosi et al*., 2013).

2.4 Viscosity

The mantle deforms according to both linear diffusion creep and non-linear dislocation creep mechanisms; however, to limit the number of variables present in this study, in all but one case I assume that the mantle deforms by diffusion creep

$$\eta_{diff} = 0.5 \mathrm{A}_{diff,j}^{-1} \mathrm{d}_{,j}^{m} \exp\left(\frac{\left(\mathrm{E}_{diff,j}^{*} + \mathrm{PV}_{diff,j}^{*}\right)}{RT}\right), \tag{16}$$

where R is the gas constant, m is the grain size exponent, and A_j, d_j, E^*_j, and V^*_j are the phase dependent constant prefactor, constant grain size, activation energy, and activation volume for a given phase j. Values of the activation energy for each phase were chosen

within experimental ranges (*Hirth and Kohlstedt*, 2003; *Shimojuku et al*., 2004; *Yamazaki and Karato*, 2001; Table 2.2). To avoid complications associated with a constantly growing cold, upper thermal boundary layer (TBL), the model upper surface is set to a depth of 35 km in the mantle, which results in decreased upper mantle viscosities. To maintain viscosities similar to those expected from seismic and glacial rebound studies (*Lambeck and Johnston* 1998; *Mitrovica and Forte* 2004), I decrease the upper mantle activation volume from $6x10^{-6}$ m^3 mol^{-1} to $3x10^{-6}$ m^3 mol^{-1}. Constant grain sizes were chosen for each phase based upon average grain sizes determined from dynamic models simulating grain size evolution in whole mantle convection (*Dannberg et al*., 2017). I note that the uppermost mantle grain size of 2.235 mm is lower than expected for depths <240 km (6-14 mm) (*Ave Lallement et al*., 1980), and grain sizes at greater depths are not well constrained, making comparisons to experimental values difficult. Constant prefactor values were chosen to match the magnitudes of observationally-based viscosity profiles for the Earth (e.g., *Steinberger and Calderwood*, 2006; Figure 2.3).

In this study, I include temperature jumps associated with latent heat release during phase changes in the temperature reference profile. The temperature jumps depend on the Clapeyron slope, resulting in small differences in reference temperature profiles between models. To account for this in the viscosity profile, I create a reference profile with phase transition Clapeyron slopes of 2 MPa K^{-1} for the 410 km transition, and -2 MPa K^{-1} for the 660 km transition. In runs with different Clapeyron slopes, the viscosity prefactor was varied to account for the above changes in temperature (Table 2.3), but activation energy and activation volume were unchanged. This results in viscosity profiles that are similar between runs, but that still have small differences. The potential effects of these different profiles are addressed in the discussion.

2.5 Model Setup

To numerically simulate an isolated thermal plume, the numerical domain is set to one quadrant of a 2D annulus with a thickness of 2855 km (Figure 2.4). To isolate the effects of phase transitions on an upwelling plume, no upper TBL is included. This setup avoids the effects of constantly increasing plate thickness and flow alteration by subduction of destabilized lithosphere. Therefore, along the upper surface, I impose a surface pressure of $1.18x10^9$ Pa, equivalent to a 35 km thick lithosphere with a density of 3300 kg m^{-3}, and a

constant temperature boundary condition with T(surface) = 1600 K, equivalent to expected mantle potential temperatures (*Herzburg et al.,* 2007; *Courtier et al*., 2007).

I impose two different sets of mechanical boundary conditions; in the first set, I impose free-slip (zero shear tractions, zero normal velocity) conditions along all boundaries, and, in the second set, I impose a uniform horizontal surface velocity of 2-8 cm yr^{-1}, a free-slip inner (bottom) boundary, and mixed boundary conditions on the left and right edges of the model. On the left and right boundaries, a free-slip condition is set below 450 km depth and a linearly decreasing normal velocity (e.g., channel flow) is used to prescribe inward (left boundary) and outward (right boundary) flow (e.g., *Turcotte and Schubert*, 2014) at shallower depths. Thermally, the surface and base of the mantle are isothermal (T_{top} = 1600 K, T_{bot} = 3200 K) and the sides have zero lateral temperature gradient (no heat flux).

Initial conditions for the model include an adiabatic temperature gradient, temperature jumps from 0 K to 81.3 K and 0 K to -169.6 K (depending on the Clapeyron slope) and density jumps of 165 kg m^{-3} and 330 kg m^{-3} for the 410 km and 660 km transitions, respectively, a bottom thermal boundary layer (ΔT = 757 K above coldest temperature profile) that has evolved for 300 Myr, and a localized 600 km wide thermal perturbation centered on the bottom boundary (ΔT = 550 K) to initiate plume upwelling. The 410 km and 660 km phase transitions are included at model depths of 375 km and 625 km to account for the imposed 35 km overlying plate. Hereafter, all depths mentioned in this text will be referenced to the Earth's surface (e.g., 0 km depth), not the model surface (e.g., 35 km depth). Phase transitions widths are set to 30 km, and Clapeyron slopes are varied between 0 and 4 MPa K^{-1} and -4 and 0 MPa K^{-1} for the 410 km and 660 km, respectively. In cases where I set the transition Clapeyron slope to 0 there will be no associated density or temperature jump. However, other phase dependent variables for thermal expansivity and thermal conductivity, and viscosity if the viscosity jump is included, are considered to still change to the next phase when the phase function is greater than 50%. I maintain these changes to keep these profiles, specifically in the lower mantle, similar to observed values (*Steinberger and Calderwood*, 2006; *Tosi et al*., 2013).

2.6 Numerical Methods

ASPECT solves the Stokes system and temperature field using a combination of linear and non-linear solvers. The linear method iteratively solves approximations of a linear system until the approximation is within a tolerance of the exact solution. I use tolerances of

10^{-5} and 10^{-12} for the linear and temperature solvers respectively. Non-linearly, equations are similarly solved using an iterative approach; however, this method alternates solving the temperature and Stokes system. I allow a maximum of two non-linear iterations with a tolerance of 10^{-3}. One case is considered with tolerances lowered to 10^{-7} and 10^{-5} for the linear and non-linear solvers, and maximum non-linear iterations increased to four to ensure observed dynamic accuracy. Timesteps are limited by the Courant-Fredrichs-Lewy (CFL) condition. In these models the CFL is set to one.

Adaptive mesh refinement was used. The mesh was refined every 5 timesteps based on the viscosity, non-adiabatic temperature, and a maximum refinement function. To decrease model run time, outside of the inner section of the annulus (33-57º) cell edge length was limited to ≥~40 km. The inner section was further refined, with cell size capped at ≥~20 km below 700 km and ≥~5 km at shallower depths. One case increased the maximum refinement of the upper 700 km to ~2.5 km.

3. Results

To test the role of Clapeyron slopes, plate motion rates, and phase transition depth on dynamic variability in plume upwelling rates, I ran models with Clapeyron slopes of 0 to 4 MPa for the 410 km depth transition and -4 to 0 for the 660 km depth transition, plate motion rates between 0 and 8 cm yr^{-1} (zero plate motion velocities correspond to free-slip boundary conditions), and phase transitions 50 km or 100 km deeper than their seismically identified depths (e.g., *Flanagan and Shearer*, 1998). To assess the impact of these variables on plume upwelling, I examine several parameters including upward volume flux of plume material at three arbitrary depths of 135 km, 255 km, and 375 km, the total volume of plume material to pass through the transition zone, the average, maximum, and minimum plume temperature and plume velocity, and the tilt of the plume conduit in the upper mantle.

3.1 Runs without Imposed Surface Velocity

My simulations first examine the evolution of a rising plume without imposed surface velocities (i.e., plate motions) and a free-surface upper boundary, effectively isolating the influence of buoyancy on plume upwelling. Results are presented beginning with a simple rising plume in a uniform mantle followed by incrementally adding complexity by including a viscosity jump at 660 km followed by the thermal and physical effects of the 660 km and the 410 km phase transitions across the above range of Clapeyron slopes. For these cases, volume flux exhibits similar patterns at all depths (Figure 3.1). Thus, I only present volume flux results at 375 km depth.

3.1.1 Plume Evolution without Phase Transitions

Figure 3.2 shows the temporal evolution of plume volume flux in a simulation with a free slip top boundary condition, no phase transitions, and a viscosity structure governed by temperature and pressure (see Table 2.2 and 2.3 for parameters values). Initially, a large plume head rises through the mantle until encountering the model surface where it spreads laterally. The plume head is followed by a smaller plume conduit whose radius decreases as it rises through the mantle from ~100 km at the CMB to ~30 km in the upper mantle. The plume head results in a high initial plume flux into the upper mantle of 1.48×10^5 m^3 yr^{-1} m^{-1}, followed by a rapid decrease to 2.50×10^4 m^3 yr^{-1} m^{-1} over 2 Myr. Note that, hereafter, I refer to increases followed by rapid decreases in plume volume flux as a plume pulse.

Approximately 15 Myr after the initial plume pulse (i.e., the plume head), slower moving material within the plume stem reaches the 660 km transition causing a second pulse. Plume volume flux then wanes steadily over ~200 Myr, at which time a third pulse of plume material enters the upper mantle. This third pulse initiates after formation of new plumes at the model boundaries (Figure 3.3) perturbs the lower TBL structure.

Evidence from post-glacial rebound and the geoid suggest that mantle viscosity increases significantly between the upper and lower mantle at approximately the depth of the 660 km phase transition (e.g., *Kaufmann and Lambeck*, 2000), although some studies suggests viscosity peaks deeper in the mantle (~1000 km; *Rudolph et al*., 2015). Therefore, I next examine the impact of a ~30x viscosity jump at 660 km. Similarly to cases without a viscosity jump, the plume initially forms a large head that rises smoothly to the model surface and spreads laterally. Unlike the previous cases, however, the viscosity jump causes a sharp drop in conduit radius, from ~150 to 50 km (Figure 3.4) across a vertical distance of ~200 km, and an increase in upward plume velocity from ~0.07 m yr^{-1} to ~0.3 m yr^{-1} (Figure 3.5; *Brunet and Yuen*, 2000). As in cases without a viscosity jump, a second pulse occurs as the plume conduit establishes itself in the wake of the rising plume head; however, the second pulse occurs at a later time (~23 Myr after the initial pulse) due to the higher lower mantle viscosity (2.47×10^{22} Pa s relative to 2.26×10^{20} Pa s).

3.1.2 Plume Evolution with a 660 km Phase Transition

The next set of results examine plume dynamics in a mantle with the 660 km phase transition for Clapeyron slopes between -4 MPa K^{-1} and -1 MPa K^{-1}. Variable Clapeyron slopes result in slight differences in temperature and viscosity profiles, which can change the arrival time of plumes into the upper mantle. To directly compare between cases, I examine plume volume flux for 205 Myr, with time 0 set to 5 Myr before the plume head reaches 375 km depth. Cases with Clapeyron slopes of -2 MPa K^{-1} and -1 MPa K^{-1} evolve similarly to those without phase transitions (Figure 3.6). Clapeyron slopes <-3 MPa K^{-1} inhibit plume flow causing it to spread out beneath the 660 km phase change. The spreading plume material is anomalously warm and establishes a mid-mantle TBL. When the effective Ra for the upper mantle based upon this mid-mantle TBL reaches 1.96×10^6 secondary plumes (plumes starting at the mid-mantle) begin to form (Figure 3.7 and 3.8). Secondary plumes form roughly symmetrically about the plume center at lateral distances up to 600 km, and last between 12-25 Myr. Lower Clapeyron slopes (i.e., more negative) result in increased

ponding of plume material beneath the phase transition and more rapid destabilization of the mid-mantle TBL. For example, secondary plumes form 118 Myr after the initial plume pulse for a Clapeyron slope of -3 MPa K^{-1}, but 18 Myr after the initial plume pulse for a Clapeyron slope of -4 MPa K^{-1}.

The value of the Clapeyron slope of the 660 km phase transition strongly affects the timing and size of plume pulses in my simulations. For example, decreasing the 660 Clapeyron slope from -1 to -4 MPa K^{-1} increases the volume fluxes of the initial plume pulse from 2.01×10^5 m^3 yr^{-1} m^{-1} to 2.84×10^5 m^3 yr^{-1} m^{-1}, the initial plume head size from 360 km to 480 km, maximum plume velocity from 2.53 m yr^{-1} to 3.02 m yr^{-1}, and the maximum non-adiabatic plume temperature from 491 K to 602 K. Mean non-adiabatic plume temperature is approximately constant for values of the 660 km Clapeyron slope from -3 MPa K^{-1} to -1 MPa K^{-1} at ~216 K, but drops to 188 K when the Clapeyron slope is -4 MPa K^{-1} (Table 3.1). Increasing the Clapeyron slope at the 660 km phase transition from -4 MPa K^{-1} to -1 MPa K^{-1} causes the arrival of the second plume pulse to shift from 28 Myr to 15 Myr after the initial pulse and to decrease in size from 8.2×10^4 m^3 yr^{-1} m^{-1} to 6.2×10^4 m^3 yr^{-1} m^{-1}.

3.1.3 Plume Evolution with both the 660 km and 410 km Phase Transition

The addition of the 410 km phase transition causes minor changes to the overall plume dynamics. For cases with a 660 km Clapeyron slope of -2 MPa K^{-1} and -1 MPa K^{-1}, all values for the 410 km phase transition evolve similarly to those without the 410 km transition. Notable differences from increasing the 410 km transition Clapeyron slope from 1 MPa K^{-1} to 4 MPa K^{-1} include a smaller initial plume head diameter (282 km to 214 km), lower maximum volume fluxes of the initial pulse (1.6×10^5 m^3 yr^{-1} m^{-1} to 1.2×10^5 m^3 yr^{-1} m^{-1}), and a smaller (3.8×10^4 m^3 yr^{-1} m^{-1} instead of 4.9×10^4 m^3 yr^{-1} m^{-1}), delayed second pulse (54 Myr instead of 41 Myr) (Figure 3.9). As in cases without the 410 km transition, a 660 km Clapeyron slope of -3 MPa K^{-1} inhibits plume upwelling and forms a TBL, however, addition of the 410 km phase transition yields a single plume in the upper mantle that behaves similar to runs with a -2 MPa K^{-1} and -1 MPa K^{-1} 660 km depth Clapeyron slope, except with minor variability for the first ~80 Myr (Figure 3.10). Secondary plume formation doesn't occur until Clapeyron slope values are <-3.2 MPa K^{-1}. As the 410 km Clapeyron slope increases the max and mean plume upwelling velocity decrease 17.9% and 16.8%, the mean ΔT decreases 4.6%, and total volume of plume material decreases 6.2% (for a 660 Clapeyron of -1 MPa K^{-1}).

Next, I compare volume flux and plume location in runs with a Clapeyron slope of -4 MPa K^{-1} for the 660 km phase change and a range of Clapeyron slopes for the 410 km phase change. In all these cases, secondary plumes initially form ~350-400 km from the model center 27-33 Myr after the initial plume pulse. Runs with a 410 km Clapeyron slope of 1 to 3 MPa K^{-1} exhibit relatively similar behavior with secondary plumes forming symmetrically around the plume center and lasting for 4-50 Myr. (Figure 3.11). At a 410 km depth Clapeyron slope of 4 MPa K^{-1}, however, fewer secondary plumes form and their duration increases from ~27 Myr to up to 50 Myr (Figure 3.12).

3.2 Runs with Imposed Surface Velocity

Below, I present simulation results for cases with imposed surface velocities of 8 cm yr^{-1}. I start by presenting results of the evolution of a simple rising plume in a uniform mantle, with and without the 660 km viscosity jump, followed by the thermal and physical effects of both the 660 km and the 410 km phase transitions. Finally, a restricted set of models examine the role of phase transition depth and differing plate velocities from 2 cm yr^{-1} to 8 cm yr^{-1}. The plume flux in all of the cases below shows an initially similar pattern to cases without plate motions: an initial pulse associated with the plume head followed by a second pulse as slower moving material within the plume stem reaches 660 km depth. Here, I discuss model evolution after this second pulse.

3.2.1 Plume Evolution without Phase Transitions

First, I examine a model with imposed plate motions, but no phase transitions and no viscosity jump at 660 km (Figure 3.13). In this case, the plume reaches the upper mantle and then tilts in the direction of plate motion. Tilting is most pronounced in the upper mantle, where the average viscosity is lower (2.25×10^{20} Pa s) than in the lower mantle (1.1×10^{22} Pa s) and plate motion causes lateral advection of plume material. Near the surface, the plume conduit tilts to near horizontal (~88º from vertical) after ~70 Myr. As the plume tilts, the conduit radius increases (~37 km to ~65 km) until a small pulse rises and reorients the conduit to ~63º from vertical. This process then repeats; the plume conduit slowly tilts to near horizontal while thickening until a new instability forms causing a pulse which re-orients the conduit. Although tilting is primarily restricted to the upper 250 km of the mantle, small

changes in plume volume flux and plume tilt precede these pulses by ~3.5 Myr at 375 km depth (Figure 3.14). These pulses continue throughout the model run.

Cases with a ~30x viscosity jump between the upper and lower mantle at 660 km depth primarily restrict plate driven flow to the upper mantle. Consequently, plume conduit tilting is almost entirely restricted to the upper mantle. Otherwise, the plume conduit behavior is similar to cases without a viscosity jump: mantle flow causes the plume conduit to tilt to near horizontal leading to an increase in plume conduit radius (~25 to 60 km) and a subsequent pulse.

3.2.2 Plume Evolution with the 660 km and 410 km Phase Transitions

Figure 3.15 shows a volume flux comparison at depths of 135 km, 255 km, and 375 km with a Clapeyron slope of -1 MPa K^{-1} for the 660 km phase transition and 1 MPa K^{-1} for the 410 km phase transition. Models with a Clapeyron slope of -2 and -1 MPa K^{-1} for the 660 km phase transition behave similarly to those with no phase transitions, except with the addition of the 410 km transition an initial pulse forms at the 660 km transition when a tilt of ~73º is reached. This pulse similarly occurs with an increase in plume conduit radius as the tilt from vertical increases, and in some cases, can reorient the plume to vertical. Higher 410 km transition Clapeyron slopes result in more pulses from 660 km that spread over a longer time span (Figure 3.16). Secondary pulses occur at a similar time after the initial pulse regardless of the 410 km transition, but occur sooner with decreasing 660 Clapeyron slope up to -3 MPa K^{-1} (37, 31, 24, and 29 Myr after initial plume pulse for -1, -2, -3, and -4 MPa K^{-1} respectively). Although pulsing in the uppermost mantle begins similarly to models without phase transitions, pulsing starts later with decreasing 660 Clapeyron slope (70 Myr and 88 Myr for -1 MPa K^{-1} and -2 MPa K^{-1}), and sooner with increasing 410 Clapeyron slope (70 Myr and 40 Myr for 1 MPa K^{-1} and 4 MPa K^{-1}; Table 3.2).

For Clapeyron slopes <-3 MPa K^{-1}, the initial pulse from the 660 km phase transition seen in earlier runs instead initiates a second plume (Figure 3.17). Formation of the second plume occurs after the main plume conduit drifts along the mid-mantle TBL in the direction of plate motion. The second plume forms at the left-hand edge of the mid-mantle TBL (Figure 3.18), causing upwelling in the initial plume to cease. The process commonly repeats, but for horizontally narrow TBLs (<350 km lateral width), the secondary plume merges with the initial plume causing a large volume flux pulse. The narrower the TBL the greater the depth at

which the plumes merge. Secondary plumes form irregularly between 6.3 Myr and 54.1 Myr, at Clapeyron slopes for the 660 km phase transition of -4 MPa K^{-1} and -3 MPa K^{-1}. At -3 MPa K^{-1}, ~4-7 secondary plumes formed, regardless of the 410 km phase transition Clapeyron slope. These secondary plumes formed up to 800 km apart with durations up to 111 Myr. Increasing Clapeyron slopes for the 410 km phase transition from 1 MPa K^{-1} to 4 MPa K^{-1} decreased from 43 Myr to 15 Myr the period over which two secondary plumes coexist (Figure 3.19). For all 410 km transition Clapeyron slope values decreasing the 660 km transition's Clapeyron slope to -4 MPa K^{-1} lowered the period of secondary plume coexistence to ~21 Myr and the maximum duration of each secondary plume to a maximum of 63 Myr (Table 3.3).

3.3 The Role of Surface Velocity

To examine the impact of plate velocity on plume dynamics, I ran a restricted series of models with surface velocities of 2, 4, 6, and 8 cm yr^{-1} with Clapeyron slopes of 4 MPa K^{-1} and -1 MPa K^{-1} for the 410 and 660 km phase transitions, respectively. With velocities >2 cm yr^{-1} plume pulsing occurs in the upper mantle. Tilting of the plume conduit in the uppermost mantle increases with increasing surface velocities from ~45º at 2 cm yr^{-1} to nearly horizontal at 8 cm yr^{-1}. Faster surface velocities decrease the time for pulsing to start and increase pulse magnitude and variability. No pulsing occurs for surface velocities of 2 cm yr^{-1}, and pulsing begins at 161 Myr, 99 Myr, and 40 Myr for 4 cm yr^{-1}, 6 cm yr^{-1}, and 8 cm yr^{-1}, respectively.

3.4 Increasing Transition Depth

Finally, I ran two simulations where the depth of the phase transitions are increased by either 50 km or 100 km (I still refer to them as the 410 km and 660 km phase transition for simplicity). For these models, the Clapeyron slopes are set to 4 MPa K^{-1} and -1 MPa K^{-1} for the 410 km and 660 km phase transitions and the surface plate velocity to 8 cm yr^{-1}. Variable plume volume flux related to pulsing at the 660 km transition and in the uppermost mantle is seen in all cases, and starts at a similar time (~40 Myr). However, with greater depth uppermost mantle pulsing occurs deeper, and fewer pulses originate from the 660 km transition.

4. Discussion

4.1 Variable viscosity and temperature profiles

A fundamental part of the model setup is the inclusion of thermal and physical effect of phase transitions. However, the temperature jumps related to different Clapeyron slopes cause small variations in the initial temperature profile, and, thus, viscosity profile (Figure 2.1). The primary cause of these differences is the different latent heat release for different Clapeyron slopes. As a plume passes the 660 km transition, heat is released, increasing the plume temperature and enhancing its buoyancy; the opposite happens at the 410 km transition where heat is lost to the phase change cooling the plume material. The amount of heating or cooling increases with the magnitude of the Clapeyron slope (Equations 12 and 13). The resulting small differences in the initial temperature and viscosity profiles could affect plume dynamics in the upper mantle, particularly due to their impact on plume buoyancy and flow rates. Indeed, I observe increasing max and mean plume velocities and mean ΔT (difference between plume and ambient mantle temperatures) with decreasing 660 km or increasing 410 km Clapeyron slopes. Similar results occur for higher plume temperatures associated with lower 660 km Clapeyron slopes and higher 410 km Clapeyron slopes (Table 3.1). For the viscosity profile, to account for changes in temperature I vary only the constant prefactor, and keep temperature and pressure dependences the same. This results in very similar upper mantle viscosities between runs. However, lower mantle viscosities vary, with colder temperature profiles resulting in lower viscosities in the lower mantle. These lower viscosities result in plumes reaching the upper mantle faster, and cooling less, however upper mantle dynamics remain similar in all cases.

To quantify the differences in initial plume temperature on the system evolution, I ran two models without imposed plate motions where I changed the initial plume temperature: one where I increased and one where I decreased initial plume temperature by 50 K (Figure 4.1). Increasing the initial plume temperature decreases the volume flux for the initial and second pulse. These changes are similar to the effect of an increased 410 km transition Clapeyron slope (colder plume temperatures) and a decreased 660 km transition Clapeyron slopes (warmer plume temperatures), although not as significant. For runs with an imposed surface velocity, colder plumes due to higher 410 km Clapeyron slopes result in more initial pulses from the 660 km transition spread over a longer period of time, and upper mantle pulsing begins earlier in the model (Table 3.2). However, overall plume dynamics in all runs are similar, with pulsing occurring regardless of initial plume temperatures, and with similar

periodicities. Thus, I conclude that the small differences in initial temperature and viscosity profiles have little effect on my results.

4.2 Secondary Plumes in East Africa and Iceland

When the 660 km transition Clapeyron slope exceeds a critical value (~-3.2 MPa K^{-1} without plate motions and -3.0 MPa K^{-1} with plate motions), upwelling plume material is inhibited sufficiently to spread laterally beneath the 660 km phase transition and to form a new TBL. Instabilities in this new TBL can form secondary plumes (i.e., plumes not associated with the primary lower mantle upwelling). The extent of the TBL depends on the magnitude of the Clapeyron slope, which governs the lateral extent of spreading plume material beneath the 660 km phase change. Secondary plumes rising from this new mid-mantle TBL often form in pairs separated by 200-1200 km, with the inter-plume distance decreasing throughout model runs. These distances are similar to those estimated from laboratory experiments (500-1200 km) [*Kumagi et al.,* 2007]. Secondary plumes can coexist (i.e., two or more plumes simultaneously) for up to ~43 Myr.

Recent seismic observations reveal two locations where plumes, although apparently separate at the surface, likely connect at mid-mantle depths: the northern East-African rift *(Civiero et al*., 2015), and the Iceland and Jan Mayan hotspots (*Rickers et al*., 2013). Beneath the East-African rift, *Civiero et al.* [2015] use tomographic data to identify two ~100-200 km diameter low velocity bodies separated by ~500-800 km and extending to ~700 km depth. Although the low velocity structures appear to originate deeper than 700 km, imaged upper mantle structures are smaller in scale than proposed lower-mantle plumes in the region (*Ritsema et al.*, 1999; *Montelli et al.,* 2006; *Chang and Van der Lee*, 2011; *Hansen et al.*, 2012). Plume material may be ponding, and secondary plumes forming from this material [*Civiero et al.,* 2015].

Examining shear wave velocities of the North Atlantic mantle, *Rickers et al.* [2013] found structures similar to those beneath the East-African rift. They interpret tomographic results as showing two low velocity structures within the upper mantle, one beneath Iceland and the other beneath the Jan Mayen hotspot. Although ~900 km apart on the surface, these structures appear to connect beneath the transition zone. Each low-velocity body has a diameter of ~300-400 km in the lower mantle and a smaller ~100-200 km diameter in the upper mantle, similar to the above observations beneath the MER and Afar. A decrease in

plume conduit diameter is a well-known result of a viscosity jump between the lower and upper mantle.

The above seismic observations suggest that upper mantle plumes beneath the East-African rift and North Atlantic may connect near the transition zone. The spacing between these plumes are within the range found in this study (~200-1200 km), suggesting that if the 660 km Clapeyron slope is sufficiently low (<-3.0 MPa K^{-1} or <-3.2 MPa K^{-1} depending on plate motion), ponding material could form a regional TBL from which secondary plumes initiate. Interestingly, seismic images suggest that the Jan Mayen plume branches at ~500 km depth, much shallower than observed in the models presented here. However, in some simulations, secondary plumes merge at the mid-mantle TBL and the merged plume base propagates upward (Figure 4.2), which could explain such observations of a shallower branching within the transition zone. Also remarkable is that only the Iceland hotspot has documented changes in volcanic flux and that the Jan Mayen plume appears to be isotopically distinct from the Icelandic plume. Future work is needed to determine if the Jan Mayen plume pulses as well, but such differences could be related to differences in plume tilt. Finally, it may be difficult to explain an isotopically distinct Jan Mayen plume. If Iceland and Jan Mayan are connected deeper in the mantle a future examination of how chemically distinct regions of mantle could be maintained and rise in separate plumes could provide constraints on mid-mantle dynamics.

4.3 Source, depth, and periodicity of pulsing plumes

In all cases with 660 km phase transition Clapeyron slopes less than -2 MPa K^{-1}, there are temporally varying plume volume fluxes. This variability is associated with tilting of the plume conduit in two separate areas. First, at the 660 km transition, the plume conduit destabilizes for tilts >~73º, resulting in large volume flux pulses, which can reorient the plume to vertical and move the surface upwelling center up to ~600 km. These large pulses can occur coevally with the secondary pulse seen in cases with no plate motion. The number of deep pulses and time-span over which they occur are related to the Clapeyron slope of the 410 km phase transition. Higher values of the 410 km phase transition Clapeyron slope increase the number and time-span of pulses from the 660 km phase transition (Table 3.2). Second, pulses also form in the upper mantle as the plume is sheared laterally by plate motion. This upper mantle pulsing occurs in the upper ~250 km of the model when the plume conduit tilts by ~88º (Figure 4.3).

To compare modeled upper mantle plume pulses to observations at hotspots, I calculate periodograms using the Lomb-Scargle method (*Lomb*, 1976; *Scargle*, 1982) and identify spectral peaks that reach the ≥99% significance interval. Because I am focusing on upper mantle pulsing, which tends to develop at later times in model runs, I restrict the periodogram calculation to times >100 Myr after the plume enters the upper mantle (Figure 4.4, 4.5, 4.6, and 4.7). Periodicities for all cases with Clapeyron slopes for the 660 km phase transition of ≥-2 MPa K^{-1} range from 4.1 Myr to 37.9 Myr (Figure 4.8; Table 3.4), with periods of 4.1 Myr to 15.2 Myr and 4.1 Myr to 37.9 Myr for 660 Clapeyron slopes of -1 MPa K^{-1} and -2 MPa K^{-1}. Changes in the 410 km Clapeyon slope and imposed surface velocity have no noticeable effect on the periodicity. However, increasing the 410 km Clapeyron slope from 1 MPa K^{-1} to 4 MPa K^{-1} reduces the time for pulsing to start, from 70 Myr to 30 Myr. Decreasing the 660 km Clapeyron slope from -1 MPa K^{-1} to -2 MPa K^{-1} increases the time for pulsing to start from 70 Myr to 88 Myr (Table 3.2).

The periodicity of changes in volcanic production at Iceland and Hawaii are estimated to be ~5-10 Myr, and ~5-30.4 Myr, respectively (*O'Connor et al*., 2001; *Ito*, 2001; *Van Ark and Lin*, 2004; *Vidal and Bonneville*, 2004; *Wessel*, 2016). Similar periodicities are observed in this study. My results suggest that the larger range of periodicities for Hawaii is consistent with a lower 660 km Clapeyron slope of -2 MPa K^{-1}, however, the timing until pulsations begin in those models (~90 Myr) exceeds the age of the currently existing Hawaiian hotspot chain (~75 Myr; *Ito and van Keken*, 2007). Only cases with a Clapeyron slope of -1 MPa K^{-1} begin upper mantle pulsing soon enough to be present in surface expressions at Hawaii and Iceland. However, if a large pulse from the 660 km transition reorients the plume to vertical this could appear as a new hotspot at the surface. In that case, the start of upper mantle pulsing could shift forward 30-62 Myr. This would result in variability from pulsing showing in surface expression after ~0-57 Myr or ~32-67 Myr with a 660 Clapeyron slope of -1 MPa K^{-1} and -2 MPa K^{-1}, within the age of existing hotspots.

4.4 Plume Instability Mechanisms

Several mechanisms have been proposed for destabilizing plume conduits in the mantle. For example, in some cases, a tilted plume conduit may develop Rayleigh-Taylor-like instabilities that grow more rapidly than the conduit rises through the mantle (*Whitehead*, 1982). These instabilities have been proposed as a cause for temporally variable magmatic flux at hotspots (*Vidal and Bonneville*, 2004) and seismic observations suggest some plumes

exhibit tilting (e.g., Iceland; *Rickers et al*., 2013). Results from the present study demonstrate plume flux variability after destabilization of such a tilted plume conduit. However, although tilting of the conduit is required for destabilization to take place, it is not the sole process by which pulsation initiates in my models. Given sufficient time (~100 Myr), small-scale convection develops in the uppermost mantle due to the warm plume material spreading beneath the cooler model surface. In some cases, downwellings associated with small-scale convection begins "upstream" of the tilted plume conduit and the associated downwellings are advected along with plate motion towards the plume. Upon crossing over the plume, these downwellings destabilize the plume conduit and initiate pulses. After this initial destabilization, the tilted plume conduit continues to pulse periodically for the duration of the model run.

Previous work questions whether a tilted mantle plume is likely to form instabilities in the Earth's mantle (*Kerr et al*., 2008; *Meriaux et al*., 2011). Laboratory and numerical simulations of rising horizontal plume conduits find instabilities develop for Ra values between the plume conduit and surrounding mantle, Ra_{pc}, greater than 300. For Ra_{pc} values less than 300, the rate of thermal diffusion outpaces the rate of instability growth, stabilizing the plume conduit. In addition to the Ra_{pc}, another measure of instability formation in the mantle is the balance between the timescale for instability growth (the time for a diapir-like instability to grow to a size equal to the conduit diameter) and the rise time of the material through the upper mantle. Growth timescales greater than rise times provide insufficient time for an instability to form. Calculating these timescales based upon estimates of mantle parameters, *Meriaux et al.* [2011] and *Kerr et al.* [2008] both conclude that plumes should remain stable in the upper mantle regardless of tilt. However, these studies did not account for several parameters that may affect plume dynamics in the upper mantle including compressibility, phase changes, and the depth-dependence of viscosity, thermal conductivity, and thermal expansion. To evaluate the role of instability growth along tilted plume conduits in my numerical simulations, I calculate the conduit Ra_{pc}, instability growth timescale, and the rise time of material within the plume conduit following *Meriaux et al.* [2011],

$$Ra_{pc} = \frac{\Delta\rho g a^3}{\kappa \eta_m} \tag{17}$$

$$\tau_g = \frac{c\eta_m}{\Delta\rho g a} \tag{18}$$

$$t_r = \frac{h}{v_s} \tag{19}$$

where τ_g is the timescale for instability growth, t_r is the rise time, Δρ is the density difference between the plume and mantle, η_p is plume viscosity, η_m is the ambient mantle viscosity, a is the conduit radius, κ is thermal diffusivity, *c* is a dimensionless constant, *h* is the thickness of the upper mantle (600 km), and v_s is the stokes velocity

$$v_s = \frac{0.13(\eta_m/\eta_p)^{0.62}\Delta\rho g a^2}{\eta_m}. \tag{20}$$

Values of the above timescales are calculated at each time (every ~0.25 Myr). To delineate the boundaries of upwelling plumes, I arbitrarily define plume material as the portion of the mantle with a ΔT that is 30% greater than mean non-adiabatic temperature. From this, η_m is calculated as the mean viscosity outside the plume, η_p and Δρ the mean viscosity and density change of the plume, and thermal diffusivity the mean of the whole system. I solved for the constant *c* by fitting a third-degree polynomial to data provided in *Meriaux et al.* [2011] (Figure 4.9).

Because the effective radius of plume material subject to destabilizing changes with the tilt of the plume conduit, I calculate an effective plume conduit radius as

$$a_t = \frac{a}{\cos(\theta)}, \tag{21}$$

where θ is the plume conduit's tilt from vertical, and a_t the effective radius. Comparing the rise and instability growth times, there is a pattern of rise time exceeding the instability growth time (~3.7 Myr and 0.8 Myr), followed by growth time surpassing rise time (~0.12 Myr and 0.08 Myr; Figure 4.10). This pattern relates to conduit tilt and radius, as they increase both the rise and growth times decrease. However, rise time decreases more rapidly than growth time. Once a pulse has occurred and the conduit reorients its tilt to ~63º, rise time is greater than instability growth time, allowing an instability time to develop as the conduit tilts back to near horizontal.

Calculating the radius increase from the tilt as I do above, as theta approaches 90º the radius will exceed what is predicted in the mantle from mass flux calculations (26 to 52 km; *Kerr et al*., 2008). With rise time having a greater dependence on the radius, its value will be underestimated relative to growth rate at a large plume radius. By calculating the rise and growth times assuming that radius remains constant and within the range seen in this model (~25 km to 60 km), both times similarly decrease as radius increases, however the growth time never exceeds the rise time (Table 4.1). This suggests that within the range of conduit radii predicted for the mantle, there is sufficient time for an instability to grow, and that an increase in radius with tilt will cause these instabilities to form faster.

5. Conclusions

In this study I ran 2D numerical simulations to examine the effect of phase transition Clapeyron slopes with and without plate motion on mantle plume dynamics. I find that with no plate motion, regardless of the 410 km transition a plume will remain stable when the 660 km Clapeyron slope is above a critical value (>-3.2 MPa K^{-1}). Below this critical value, plume material will pond beneath the 660 km transition, forming a mid-mantle TBL where secondary plumes can initiate. By including plate motion, this critical value increases to -3.0 MPa K^{-1}. Secondary plumes form between 200-1200 km apart, which agrees with seismic observations (e.g., Iceland and the EAR).

When the 660 km Clapeyron slope is above the critical value and plate motion is included, laterally shearing of the plume conduit leads to destabilization and pulsing when a tilt of ~88º from vertical is reached. This destabilization occurs in two regions, above the 660 km transition, where destabilization causes large volume flux pulses, which in some cases, can reorient the plume conduit back to vertical and up to ~600 km away, or in the upper mantle. Upper mantle periodicities remain within a range of 4.1 Myr and 37.9 Myr regardless of Clapeyron slopes, which is similar to ranges observed at Iceland and Hawaii (5-10 Myr and 5-30.1 Myr). Upper mantle pulsing begins between 30 and 100 Myr after the plume reaches the upper mantle, with increasing time associated with lower 410 km Clapeyron slopes or higher 660 Clapeyron slopes. From this volume flux variations with periodicities similar to those observed at hotspots are seen, and in some cases, can start within the age of existing hotspots.

5.1 Future work

In this study I've shown that temporally variable volume fluxes, similar to those observed at hotspots (e.g. Hawaii), are possible from plume pulsation due to destabilization of a plume conduit. However, this study neglects important factors which may alter these dynamics such as non-linear rheology, grain-size evolution, variable plume composition, and lithosphere-plume interactions. Viscosity likely has a non-linear dependence, a single case included a harmonic average of diffusion and dislocation creep, and both pulsing at 660 km and in the upper mantle occurred similarly to those with only diffusion creep. However, because of the importance of dislocation creep in the upper mantle a more detailed analysis is required. Grain-sizes in the mantle are important in determining diffusion creep, and are thought to vary temporally (e.g., *Dannberg et al*., 2017), which may have important

implications for the evolution of plume dynamics. Observations from some plume-linked hotspots (e.g., Iceland) show compositional heterogeneity that coincides with magmatic production (*Hanan and Schilling*, 1997), which suggests there may be other mechanisms responsible for temporal magmatic variability. This study also neglects the lithosphere. Because plume destabilization is reliant on either tilt or small-scale convection, plume-lithosphere interactions could affect the timing until initiation of pulsing.

References

Akaogi, M., Ito, E., Navrotsky, A., (1989), Olivine-modified spinel–spinel transitions in the system Mg2SiO4–Fe2SiO4: CALORIMETRIC measurements, thermochemical calculation, and geophysical application. Journal of Geophysical Research 94, 15671–15685.

M. Albers, U.R. Christensen, (1996), The excess temperature of plumes rising from the core mantle boundary, Geophys. Res. Lett. 23, 3567-3570.

Ave Lallemant, H. G., J.-C. C. Mercier, N. L. Carter, and J. V. Ross, (1980), Rheology of the upper mantle: Inferences from peridotite xenoliths, Tectonophysics, 70, 85–113, doi:10.1016/0040-1951(80)90022-0.

W. Bangerth, J. Dannberg, R. Gassmöller, T. Heister, and others, (2018), ASPECT v2.0.0 pre, Computational Infrastructure for Geodynamics, 10.5281/zenodo.1297145

Beier, C., Vanderkluysen, L., Regelous, M., Mahoney, J.J., Garbe-Schönberg, D., (2011) Lithospheric control on geochemical composition along the Louisville Seamount Chain. Geochemistry, Geophysics, Geosystems, 12, 9, doi:10.1029/2011GC003690.

Bossmann, A.B. & van Keken, P.E., (2013), Dynamics of plumes in a compressible mantle with phase changes: implications for phase boundary topography, Phys. Earth planet. Inter., 224, 21–31.

Brunet, D., Yuen, D.A., (2000), Mantle plumes pinched in the transition zones. Earth Planet. Sci. Lett. 178, 13 – 27.

Chang, S.-J., and S. Van der Lee, (2011), Mantle plumes and associated flow beneath Arabia and East Africa, Earth Planet. Sci. Lett., 302(3–4), 448–454.

Christensen, U.R., Yuen, D.A., (1985), Layered convection induced by phase Transitions, J. Geophys. Res, 90, B12.

Civiero, C., Hammond, J.O.S., Goes, S., Fishwick, S., Ahmed, A., Ayele, A., Doubre, C., Goitom, B., Keir, D., Kendall, J.M., Leroy, S., Ogubazghi, G., Rümpker, G., Stuart, G.W., (2015), Multiple mantle upwellings in the transition zone beneath the northern East African Rift system from relative P-wave travel-time tomography. Geochemistry, Geophysics, Geosystems 16, 2949–2968.

M.L. Coffin, M.S. Pringle, R.A. Duncan, T.P. Gladczenko, M. Storey, (2002), Kerguelen hot spot magma output since 130 Ma, J. Petrol. 43, 1121–1139.

Courtier, A. M., et al., (2007), Correlation of seismic and petrologic thermometers suggests deep thermal anomalies beneath hotspots, Earth Planet. Sci. Lett., 264(1), 308–316.

Courtillot, V., Davaille, A., Besse, J., Stock, J., (2003), Three distinct types of hotspots in the Earth's mantle. Earth Planet. Sci. Lett. 205, 295–308.

Dannberg, J., Eilon Z., Ulrich, F., Gassmöller, R., Moulik, P., Myhill, R., (2017), The importance of grain size to mantle dynamics and seismological observations, Geochem. Geophys. Geosyst. 18, 3034-3061, doi:10.1002/2017GC006944.

Faccenda, M., & Dal Zilio, L., (2017), The role of solid–solid phase transitions in mantle convection. Lithos, 268, 198–224.

Farnetani, C.G., Samuel, H., (2005), Beyond the thermal plume paradigm. Geophys. Res. Lett. 32, L07311. doi:10.1029/2005GL022360.

Flanagan, M.P., and P.M. Shearer, (1998), Global mapping of topography on transition zone velocity discontinuities by stacking SS precursors, J. Geophys. Res., 103, 2673-2692.

French, S. W. & Romanowicz, B., (2015), Broad plumes rooted at the base of the Earth's mantle beneath major hotspots. Nature 525, 95–99.

Fukao, Y. & Obayashi, M., (2013), Subducted slabs stagnant above, penetrating through, and trapped below the 660 km discontinuity. J. Geophys. Res. 118, 1–19.

Ghosh, S., Ohtani, E., Litasov, D.K., Suzuki, A., Dobson, D., Funakoshi, K., (2013), Effect of water in depleted mantle on post-spinel transition and implication for 660 km seismic discontinuity. Earth and Planetary Science Letters 371-372, 103–111.

Hanan, B.B., Schilling, J.-G., (1997), The dynamic evolution of the Iceland mantle plume: the lead isotope perspective. Earth Planet. Sci. Lett. 151, 43–60.

Hansen, S. E., A. A. Nyblade, and M. H. Benoit, (2012), Mantle structure beneath Africa and Arabia from adaptively parameterized P-wave tomography: Implications for the origin of Cenozoic Afro-Arabian tectonism, Earth Planet. Sci. Lett., 319–320(0), 23–34.

T. Heister, J. Dannberg, R. Gassmöller, and W. Bangerth, (2017), High accuracy mantle convection simulation through modern numerical methods. II: Realistic models and problems. Geophysical Journal International, 210(2):833–851.

Herzberg, C., P. D. Asimow, N. Arndt, Y. Niu, C. Lesher, J. Fitton, M. Cheadle, and A. Saunders, (2007), Temperatures in ambient mantle and plumes: Constraints from basalts, picrites, and komatiites, Geochem. Geophys. Geosyst., 8, Q02006, doi:10.1029/2006GC001390.

Hey, R., Martinez, F., Höskuldsson, A., Benediktsdóttir, A., (2010), Propagating rift model for the V-shaped ridges south of Iceland. Geochem. Geophys. Geosyst. 11. doi:10.1029/2009GC002865.

Hey, R., Martinez, F., Höskuldsson, Á., Eason, D.E., Sleeper, J., Thordarson, S., Benediktsdóttir, Á., Merkuryev, S., (2016), Multibeam investigation of the active North Atlantic plate boundary reorganization tip. Earth and Planetary Science Letters 435, 115-123.

Hirth, G., and D. Kohlstedt, (2003), Rheology of the upper mantle and the mantle wedge: A view from the experimentalists, Geophys. Monogr. Ser., 138, 83–105.

Ito, G., (2001), Reykjanes 'V'-shaped ridges originating from a pulsing and dehydrating mantle plume, *Nature*, vol. 411, 681-684.

Ito, E., Akaogi, M., Topor, L., Navrotsky, A., (1990), Negative pressure–temperature slopes for reactions forming MgSiO3 perovskite from calorimetry. Science 249, 1275–1278.

Ito, G., van Keken, P.E., (2007), Hotspots and melting anomalies. In: Schubert, G., Bercovici, D. (Eds.), Treatise on Geophysics, vol. 7. Elsevier, pp. 371–435.

Jarvis, G.T., McKenzie, D.P., (1980), Convection in a compressible fluid with infinite Prandtl number, Fluid Mech. 96 (3), 515–583.

Katsura, T., et al., (2004), Olivine–wadsleyite transition in the system (Mg,Fe)2SiO4. Journal of Geophysical Research 109.

Kaufmann, G., Lambeck, K., (2000), Mantle dynamics, postglacial rebound and the radial viscosity profile. Physics of the Earth and Planetary Interiors 121, 301–324.

Kerr, R.C., Meriaux, C., Lister, J.R., (2008), Effect of thermal diffusion on the stability of strongly tilted mantle plume tails, J. Geophys. Res., 113, B09401, doi:10.1029/2007JB005510.

King, S.D., Lee, C., van Keken, P.E., Leng, W., Zhong, S., Tan, E., Tosi, N., Kameyama, M.C., (2010), A community benchmark for 2-D Cartesian compressible convection in the Earth's mantle, Geophys. J. Int. 180, 73–87. http://dx.doi.org/10.1111/ j.1365-246X.2009.04413.x.

M. Kronbichler, T. Heister, and W. Bangerth, (2012), High accuracy mantle convection simulation through modern numerical methods. *Geophysical Journal International*, 191:12–29.

Kumagai, I., A. Davaille, and K. Kurita, (2007), On the fate of thermally buoyant mantle plumes at density interfaces, Earth Planet. Sci. Lett., 254, 180–193, doi:10.1016/j.epsl.2006.11.029.

Lambeck, K. and P. Johnston, (1998), The viscosity of the mantle: Evidence from analyses of glacial rebound phenomena. In: The Earth's mantle, Jackson, I. (ed), Cambridge University Press, Cambridge, 461-502.

Lomb, N., (1976), Least-squares frequency analysis of unequally spaced data. Astrophys. Space Sci. 39, 447–462.

Martinez, F., and R. Hey, (2017), Propagating buoyant mantle upwelling on the Reykjanes Ridge, Earth Planet. Sci. Lett., 457, 10–22, doi: 10.1016/j.epsl.2016.09.057.

Meraux, C., Mansour, J.A., Moresi, L.N., Kerr, R.C., May, D.A., (2011), On the rise of strongly tilted mantle plume tails. Phys. Earth Planet Inter. 184 (1e2), 63e79.

Mitrovica, J. X. & Forte, A. M., (2004), A new inference of mantle viscosity based upon joint inversion of convection and glacial isostatic adjustment data. Earth Planet. Sci. Lett. 225, 177-189.

Montelli, R., Nolet, G., Dahlen, F.A., Masters, G., (2006), A catalogue of deep mantle plumes: new results from finite-frequency tomography. Geochem. Geophys. Geosyst. 7, Q11007.

Morgan, W.J., (1971), Convective plumes in the lower mantle. Nature 230, 42–43.

T. Nakakuki, H. Sato and H. Fujimoto, (1994), Interaction of the upwelling plume with the phase and chemical boundary at the 670 km discontinuity: effects of temperature-dependent viscosity, Earth Planet. Sci. L&t. 121, 369-384.

O'Connor, J.M., Stoffers, P., Wijbrans, J.R., Shannon, P.M., Morrissey, T., (2000), Evidence from episodic seamount volcanism for pulsing of the Iceland plume in the past 70 Myr. Nature 408, 954 – 958.

Olson, P., (1990), Hot spots, swells and mantle plumes, in Magma Transport and Storage, edited by M. Ryan, pp. 33–51, John Wiley, Hoboken, N. J.

Rickers, F., Fichtner, A., Trampert, J., (2013), The Iceland–Jan Mayen plume system and its impact on mantle dynamics in the North Atlantic region: evidence from full waveform inversion. Earth and Planetary Science Letters 367, 39–51.

Ritsema, J., Allen, R.M., (2003), The elusive mantle plume. Earth Planet. Sci. Lett. 207, 1–12.

Ritsema, J., H. J. v. Heijst, and J. H. Woodhouse, (1999), Complex shear wave velocity structure imaged beneath Africa and Iceland, Science, 286(5446), 1925–1928.

Scargle, J.D., (1982), Studies in astronomical time series analysis. II-Statistical aspects of spectral analysis of unevenly spaced data. Astrophys. J. 263, 835–853.

Schubert, G., Anderson, C., Goldman, P., (1995), Mantle plume interaction with endothermic phase change. J. Geophys. Res. 100, 8245-8256.

Schubert, G., P. Olson, C. Anderson, and P. Goldman, (1989), Solitary waves in mantle plumes, J. Geophys. Res., 94, 9523– 9532.

Schubert, G., Turcotte, D. & Olson, P., (2001), Mantle Convection in the Earth and Planets, Cambridge Univ. Press, Cambridge, UK.

Schubert, G., Yuen, D.A., Turcotte, D.L., (1975), Role of phase transitions in a dynamic mantle. Geophys. J.R. Astr. Soc. 42, 705–735.

Shimojuku, A., Kubo, T., Ohtani, E., Yurimoto, H., (2004), Silicon self-diffusion in wadsleyite: Implications for rheology of the mantle transition zone and subducting plates. Geophys. Res. Lett 31, 13606.

Steinberger, B., and A. R. Calderwood, (2006), Models of large-scale viscous flow in the Earth's mantle with constraints from mineral physics and surface observations, Geophys. J. Int., 167, 1461–1481, doi:10.1111/j.1365-246X.2006.03131.x.

Stixrude, L. P., Cagney, N., Lithgow-Bertelloni C. R., (2016), The role of thermodynamics in mantle convection: is mantle-layering intermittent?, American Geophysical Union, Fall General Assembly, MR24A-03.

Suzuki, A., Ohtani, E., Morishima, H., Kubo, T., Kanbe, Y., Kondo, T., Okada, T., Terasaki, H., Kato, T., Kikegawa, T., (2000), In situ determination of the phase boundary between wadsleyite and ringwoodite in Mg2SiO4. Geophysical Research Letters 27, 803–806.

Tackley, P. J., (2008), Geodynamics: Layer cake or plum pudding? Nature Geoscience, 1, 157– 158.

Tosi, N., Yuen, D.A., de Koker, N., Wentzcovitch, R.M., (2013), Mantle dynamics with pressure- and temperature-dependent thermal expansivity and conductivity, Phys. Earth Planet. Inter. 217, 48–58.

Turcotte, D., Schubert, G., (2014), Geodynamics, Cambridge Univ. Press, Cambridge, UK.

Van Ark, E. and Lin, J., (2004), Time variation in igneous volume flux of the Hawaii-Emperor hot spot seamount chain. J. Geophys. Res., 109, B11401, doi:10.1029/2003JB002949.

R.D. Van der Hilst, S. Widiyantoro, E.R. Engdahl, (1997), Evidence for deep mantle circulation from global tomography, Nature 386, 578–584.

Vanderkluysen, L., Mahoney, J.J., Koppers, A.A.P., Beier, C., Regelous, M., Gee, J., and Lonsdale, P.F., (2014), Louisville Seamount Chain: Petrogenetic processes, and geochemical evolution of the mantle source: Geochemistry Geophysics Geosystems, v. 15, p. 2380–2400, doi: 10 .1002 /2014GC005288.

Vidal, V., and A. Bonneville, (2004), Variations of the Hawaiian hot spot activity revealed by variations in the magma production rate, J. Geophys. Res., 109, B03104, doi:10.1029/2003JB002559.

Wessel, P., (2016), Regional–residual separation of bathymetry and revised estimates of Hawaii plume flux. Geophys. J. Int. 204, 932–947.

Whitehead, J., (1982), Instabilities of fluid conduits in a flowing Earth—Are plates lubricated by the asthenosphere?, Geophys. J. R. Astron. Soc., 70, 415– 433.

Wolfe, C.J., Solomon, S.C., Laske, G., Collins, J.A., Detrick, R.S., Orcutt, J.A., Bercovici, D., Hauri, E.H., (2009), Mantle shear-wave velocity structure beneath the Hawaiian hot spot. Science 326, 1388–1390.

Yamazaki, D., Karato, S.-i., (2001), Some mineral physics constraints on the rheology and geothermal structure of Earth's lower mantle. Am. Mineral. 86 (4), 385–391.

Yu, Y.G., Wu, Z., Wentzcovitch, R.M., (2008), Alpha–beta–gamma transformations in Mg2SiO4 in Earth's transition zone. Earth planet. Science Letters 273, 115–122.

Zhao, D., (2004), Global tomographic images of mantle plumes and subducting slabs: insight into deep Earth dynamics. Phys. Earth Planet. Int. 146, 3–34.

Zhao, D., (2007), Seismic images under 60 hotspots: search for mantle plumes. Gondwana Research 12, 335–355.

Zhao, D., Yamamoto, Y., Yanada, T., (2013), Global mantle heterogeneity and its influence on teleseismic regional tomography. Gondwana Research 23, 595–616.

Tables

Table 2.1 Reference parameters used in all model runs

Symbol	Parameter	Reference value
ρ_{ref}	Reference density	3330 kg m^{-3}
T_{ref}	Surface temperature	1600 K
Cp	Specific heat capacity	1250 J kg^{-1} K^{-1}
α_{ref}	Reference thermal expansivity	$2.189 \cdot 10^{-5}$ 1 K^{-1}
K	Mantle compressibility	$4 \cdot 10^{-12}$ Pa^{-1}
d	Transition width	30 km
m	Grain size exponent	3

Table 2.2 Phase dependent parameters that change values when Γ equals 0.5.

Symbol	Parameter	Uppermost mantle	Transition zone	Lower mantle
E^*	Activation energy (J mol^{-1})	375000	231000	299000
V^*	Activation volume (m^3 mol^{-1})	$3 \cdot 10^{-6}$	$3 \cdot 10^{-6}$	$2 \cdot 10^{-6}$*
d	Grain size (m)	$2.235 \cdot 10^{-3}$	$8.18 \cdot 10^{-4}$	$2.6 \cdot 10^{-5}$
a_0	a0	$3.15 \cdot 10^{-5}$	$2.84 \cdot 10^{-5}$	$2.68 \cdot 10^{-5}$
a_1	a1	$1.02 \cdot 10^{-8}$	$6.49 \cdot 10^{-9}$	$2.77 \cdot 10^{-9}$
a_2	a2	-0.76	-0.88	-1.21
a_3	a3	$3.63 \cdot 10^{-2}$	$2.61 \cdot 10^{-2}$	$8.63 \cdot 10^{-3}$
c_0	c0	2.47	3.81	3.48
c_1	c1	0.33	0.34	0.12
c_2	c2	0.48	0.56	0.31

*In cases with a smooth viscosity profile this value is changed to $3 \cdot 10^{-6}$

Table 2.3 Phase dependent constant prefactor values for each Clapeyron slope used in model runs.

410 km transition Clapeyron slope (MPa K^{-1})	660 km transition Clapeyron slope (MPa K^{-1})	Uppermost mantle	Transition zone	Lower mantle
0	**0***	$2.750 \cdot 10^{-16}$	$5.860 \cdot 10^{-22}$	$1.700 \cdot 10^{-24}$
0	**0**	$2.750 \cdot 10^{-16}$	$5.860 \cdot 10^{-22}$	$1.438 \cdot 10^{-26}$
0	**-1**	$2.750 \cdot 10^{-16}$	$5.860 \cdot 10^{-22}$	$2.540 \cdot 10^{-26}$
0	**-2**	$2.750 \cdot 10^{-16}$	$5.860 \cdot 10^{-22}$	$4.600 \cdot 10^{-26}$
0	**-3**	$2.750 \cdot 10^{-16}$	$5.860 \cdot 10^{-22}$	$8.620 \cdot 10^{-26}$
0	**-4**	$2.750 \cdot 10^{-16}$	$5.860 \cdot 10^{-22}$	$1.670 \cdot 10^{-25}$
1	**-1**	$2.750 \cdot 10^{-16}$	$4.675 \cdot 10^{-22}$	$1.927 \cdot 10^{-26}$
1	**-2**	$2.750 \cdot 10^{-16}$	$4.675 \cdot 10^{-22}$	$3.448 \cdot 10^{-26}$
1	**-3**	$2.750 \cdot 10^{-16}$	$4.675 \cdot 10^{-22}$	$6.357 \cdot 10^{-26}$
1	**-4**	$2.750 \cdot 10^{-16}$	$4.675 \cdot 10^{-22}$	$1.210 \cdot 10^{-25}$
2	**-1**	$2.750 \cdot 10^{-16}$	$3.750 \cdot 10^{-22}$	$1.472 \cdot 10^{-26}$
2	**-2**	$2.750 \cdot 10^{-16}$	$3.750 \cdot 10^{-22}$	$2.600 \cdot 10^{-26}$
2	**-3**	$2.750 \cdot 10^{-16}$	$3.750 \cdot 10^{-22}$	$4.725 \cdot 10^{-26}$
2	**-4**	$2.750 \cdot 10^{-16}$	$3.750 \cdot 10^{-22}$	$8.853 \cdot 10^{-26}$
3	**-1**	$2.750 \cdot 10^{-16}$	$3.023 \cdot 10^{-22}$	$1.132 \cdot 10^{-26}$
3	**-2**	$2.750 \cdot 10^{-16}$	$3.023 \cdot 10^{-22}$	$1.973 \cdot 10^{-26}$
3	**-3**	$2.750 \cdot 10^{-16}$	$3.023 \cdot 10^{-22}$	$3.536 \cdot 10^{-26}$
3	**-4**	$2.750 \cdot 10^{-16}$	$3.023 \cdot 10^{-22}$	$6.527 \cdot 10^{-26}$
4	**-1**	$2.750 \cdot 10^{-16}$	$2.449 \cdot 10^{-22}$	$8.752 \cdot 10^{-27}$
4	**-2**	$2.750 \cdot 10^{-16}$	$2.449 \cdot 10^{-22}$	$1.507 \cdot 10^{-26}$
4	**-3**	$2.750 \cdot 10^{-16}$	$2.449 \cdot 10^{-22}$	$2.665 \cdot 10^{-26}$
4	**-4**	$2.750 \cdot 10^{-16}$	$2.449 \cdot 10^{-22}$	$4.848 \cdot 10^{-26}$

*No viscosity jump at 660 km depth

Table 3.1 Temperature, velocity, and volume flux statistics for all runs with no plate motion, ΔT represents the non-adiabatic temperature.

410 km transition Clapeyron slope (MPa K^{-1})	660 km transition Clapeyron slope (MPa K^{-1})	Maximum velocity (m yr^{-1})	Minimum velocity (m yr^{-1})	Mean velocity (m yr^{-1})	Maximum ΔT (K)	Minimum ΔT (K)	Mean ΔT (K)	Total volume (km^3)
0	**-1**	2.53	0.09	0.26	491	117	210	23.27
0	**-2**	2.78	0.09	0.27	526	111	220	22.71
0	**-3**	2.96	-0.03	0.21	572	69	219	23.52
0	**-4**	3.02	-0.08	0.16	602	42	188	19.70
1	**-1**	2.47	0.01	0.26	475	106	197	22.59
1	**-2**	2.87	-0.04	0.27	503	88	203	22.21
1	**-3**	3.09	0.04	0.28	520	66	204	22.20
1	**-4**	3.12	-0.07	0.16	542	26	187	21.39
2	**-1**	2.37	0.01	0.26	428	74	179	22.35
2	**-2**	2.77	-0.01	0.27	460	70	185	22.09
2	**-3**	3.15	-0.06	0.28	508	64	194	21.27
2	**-4**	2.96	-0.09	0.16	524	40	185	21.21
3	**-1**	2.26	0.04	0.27	431	72	170	21.83
3	**-2**	2.71	0.07	0.27	453	68	179	21.68
3	**-3**	3.01	0.05	0.28	479	56	182	21.08
3	**-4**	2.60	-0.06	0.13	491	15	182	20.47
4	**-1**	2.057	0.047	0.251	387.956	66.131	162.153	21.181
4	**-2**	2.533	0.023	0.265	437.915	58.072	166.858	21.267
4	**-3**	2.915	-0.035	0.275	443.401	51.729	173.819	20.882
4	**-4**	2.337	-0.087	0.186	455.499	26.503	178.898	19.825

Table 3.2 Statistics on the range and number of pulses from 660 km, and when upper mantle pulsing begins.

410 km transition Clapeyron slope (MPa K^{-1})	660 km transition Clapeyron slope (MPa K^{-1})	Period over which 660 km pulses form (Myr)	Number of 660 km pulses	Start of upper mantle pulsing (Myr)
1	**-1**	37-45	2	70
2	**-1**	38-62	4	62
3	**-1**	41-57	4	98
4	**-1**	30-95	10	30*
1	**-2**	32	1	88
2	**-2**	31-51	2	93
3	**-2**	33-61	3	100
4	**-2**	30-54	3	86

*Pulses from the 660 and upper mantle pulsing overlap in this case.

Table 3.3 Secondary plume statistics for the maximum laterally distance between plumes, longest and shortest lived secondary plumes, and maximum time two plumes coexisted for at 375 km depth.

410 km transition Clapeyron slope (MPa K^{-1})	660 km transition Clapeyron slope (MPa K^{-1})	Maximum spacing (km)	Longest plume (Myr)	Shortest Plume (Myr)	Maximum coexistence of two plumes (Myr)
No plate motion					
0	**-3**	400	20	4	12
0	**-4**	1200	29	5	29
1	**-4**	1200	30	5	30
2	**-4**	1200	25	5	25
3	**-4**	1100	24	8	24
4	**-4**	800	50	7	25
Plate motion					
1	**-3**	600	74	7	43
2	**-3**	800	100	15	32
3	**-3**	600	111	14	20
4	**-3**	700	103	4	15
1	**-4**	800	44	10	26
2	**-4**	800	33	6	18
3	**-4**	800	38	13	21
4	**-4**	700	63	10	20

Table 3.4 Table showing the minimum and maximum peak, and total number of periodicity peaks above a 99% significance interval for runs with a 660 Clapeyron slope of -1 MPa K^{-1} or -2 MPa K^{-1}

410 km transition Clapeyron slope (MPa K^{-1})	**660 km transition Clapeyron slope (MPa K^{-1})**	**Minimum peak (Myr)**	**Maximum peak (Myr)**	**Number of peaks**
1	**-1**	4.1	15.3	5
2	**-1**	4.4	9.3	5
3	**-1**	5.7	6.3	2
4	**-1**	4.5	13.8	7
1	**-2**	4.2	33.3	2
2	**-2**	4.3	24.9	7
3	**-2**	4.9	36.3	4
4	**-2**	4.5	39.9	7

Table 4.1 Mean values of the dimensionless constant c, viscosity ratio, Ra, growth time, and growth rate for a plume. In all cases, the height of the mantle was considered 600 km, and the radius was kept constant.

Radius (km)	**c**	**Viscosity ratio**	**Ra**	**Growth time**	**Rise time**
25	21.5	6.8	42	17.5	48.3
42	13.7	6.8	199	6.7	17.1
60	5.5	6.8	580	1.9	8.4

Figures

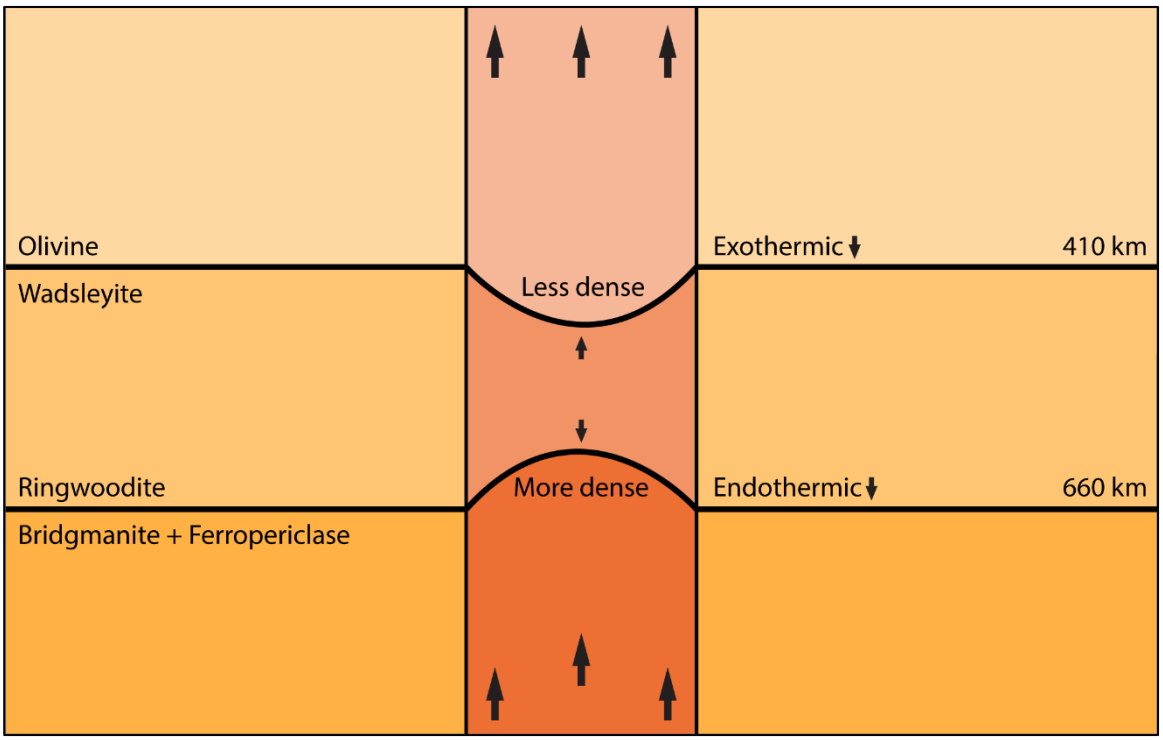

Figure 1.1 Diagram showing the deflection and effects of the 410 km and 660 km on an upwelling mantle plume.

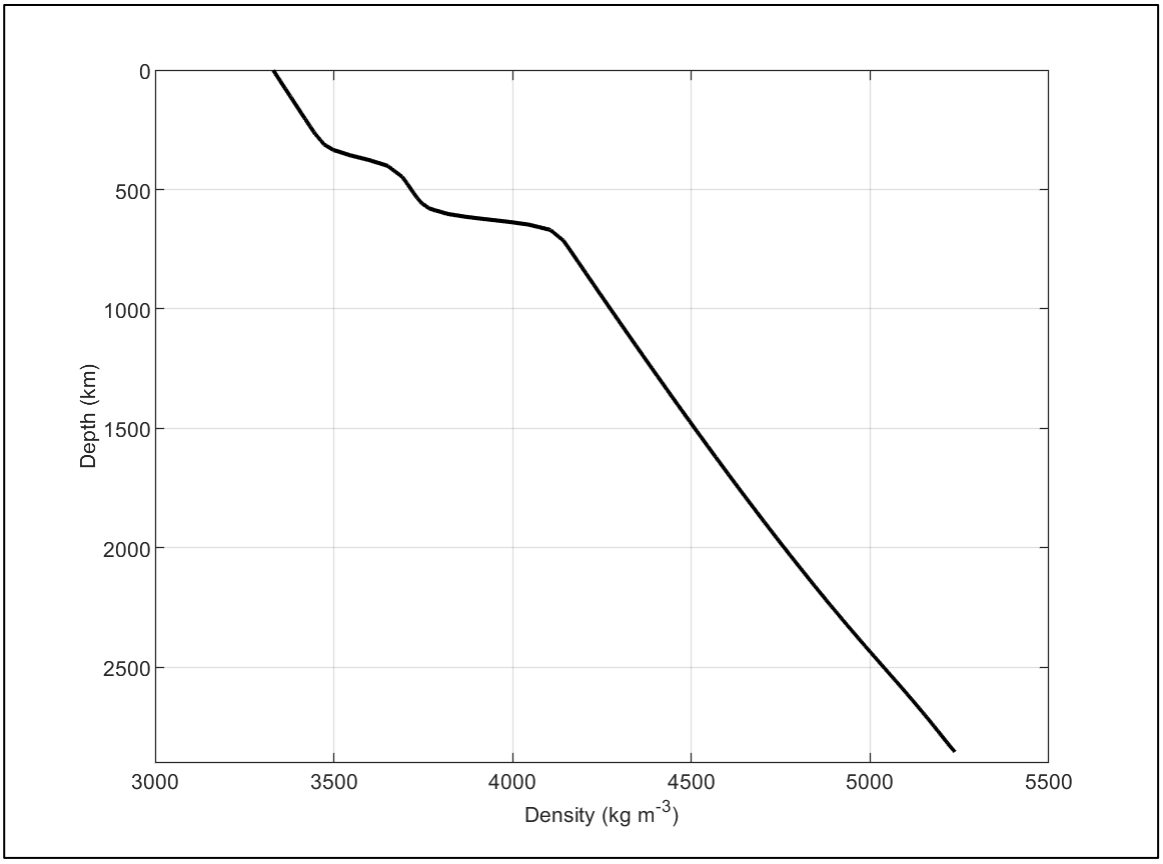

Figure 2.1 Reference density profile with depth, including density jumps of 165 kg m^{-3} and 330 kg m^{-3} at the 410 km and 660 km phase transitions.

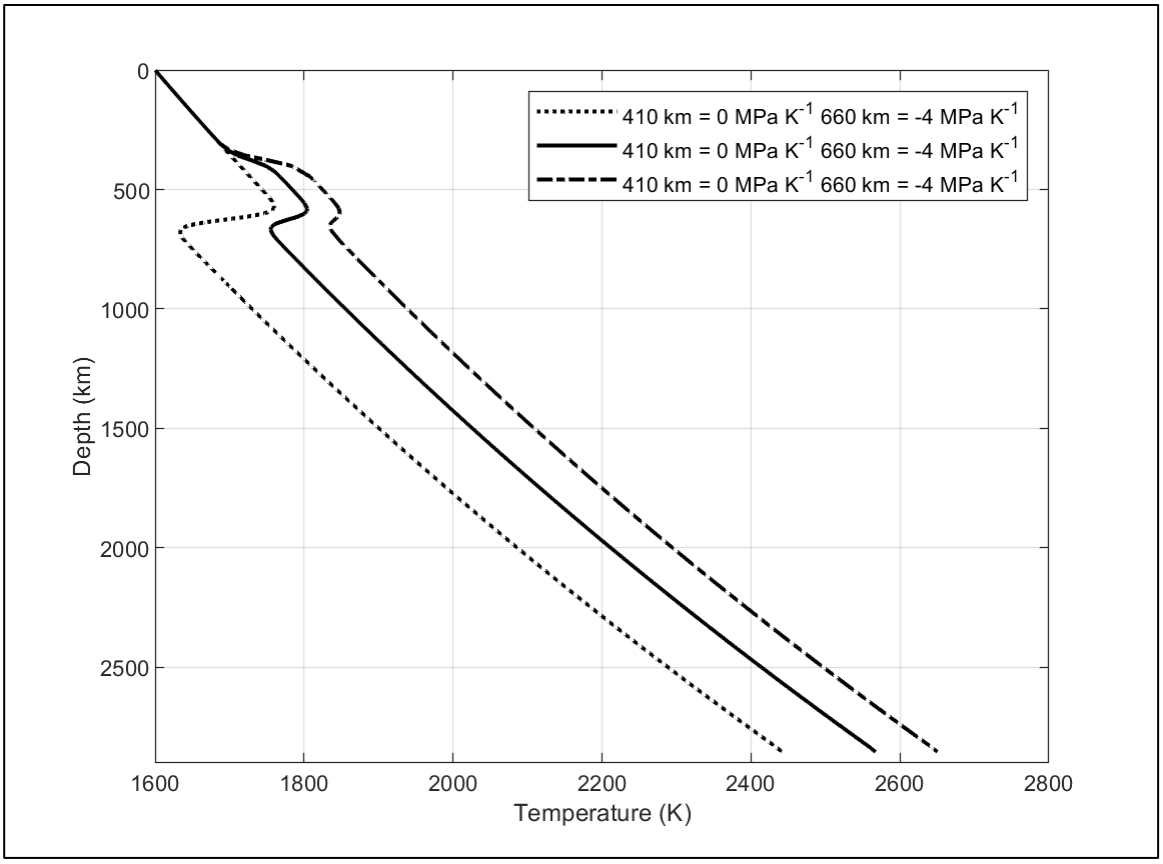

Figure 2.2 Maximum, reference, and minimum temperature profiles when not including the bottom boundary TBL. The dotted line represents the minimum temperature profile, the solid line the reference, and the dashed line maximum temperature

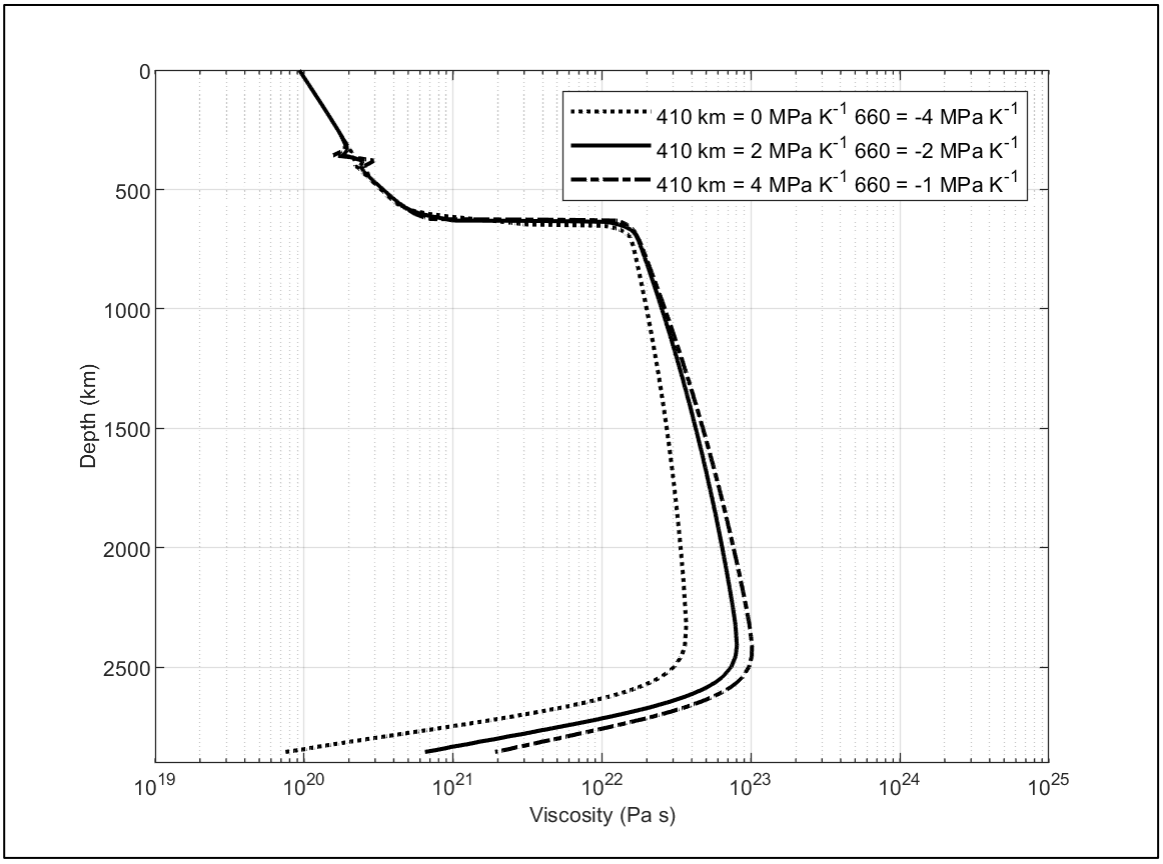

Figure 2.3 Associated viscosity profile for the minimum (dotted line), reference (solid line), and maximum (dashed line) temperature profiles.

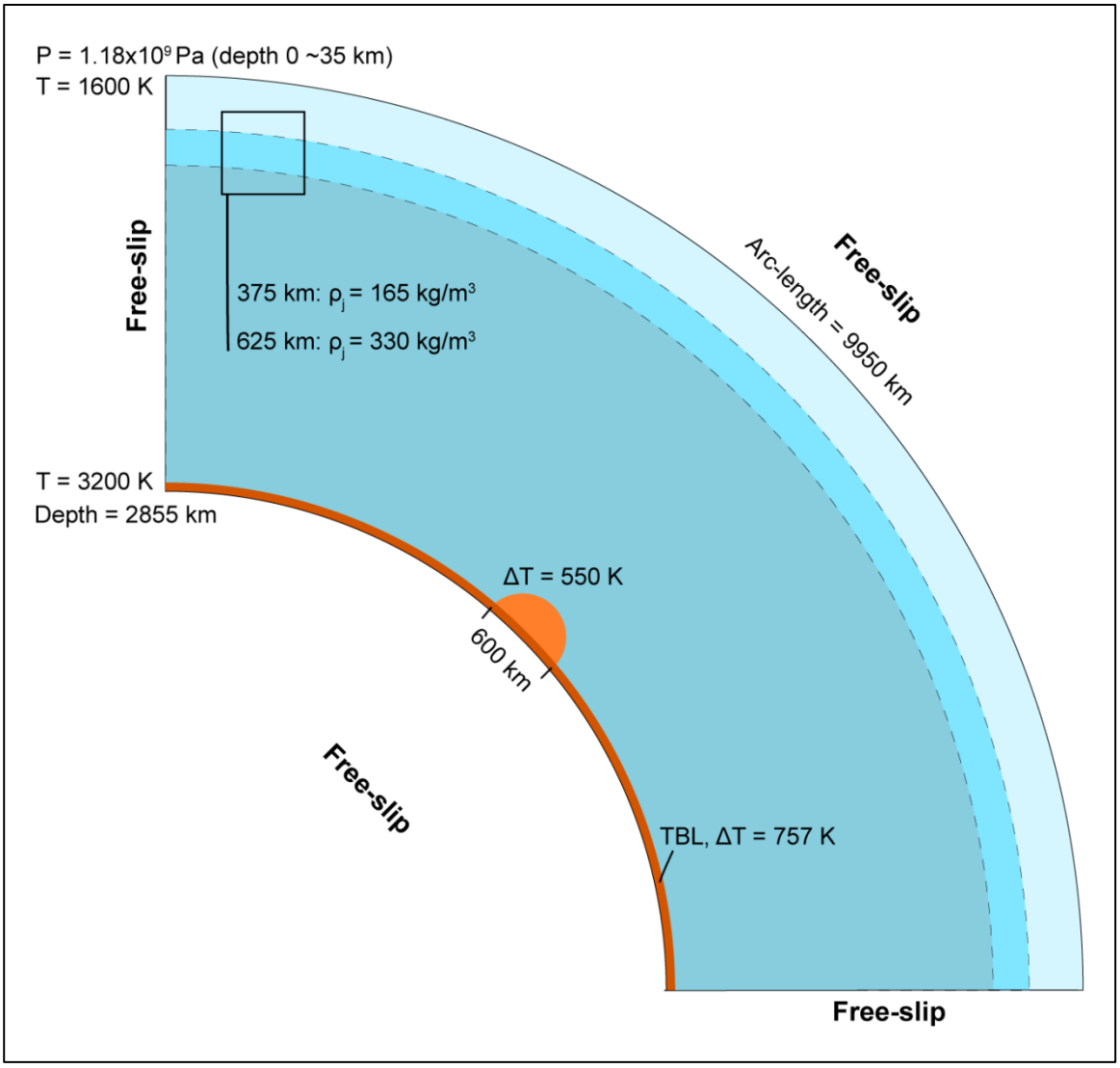

Figure 2.4 Diagram showing the general model setup with two phase transitions at 410 km and 660 km, and no imposed surface velocity. Blue colors indicate the different mantle phases, dark orange the bottom boundary TBL, and light orange the initial plume material.

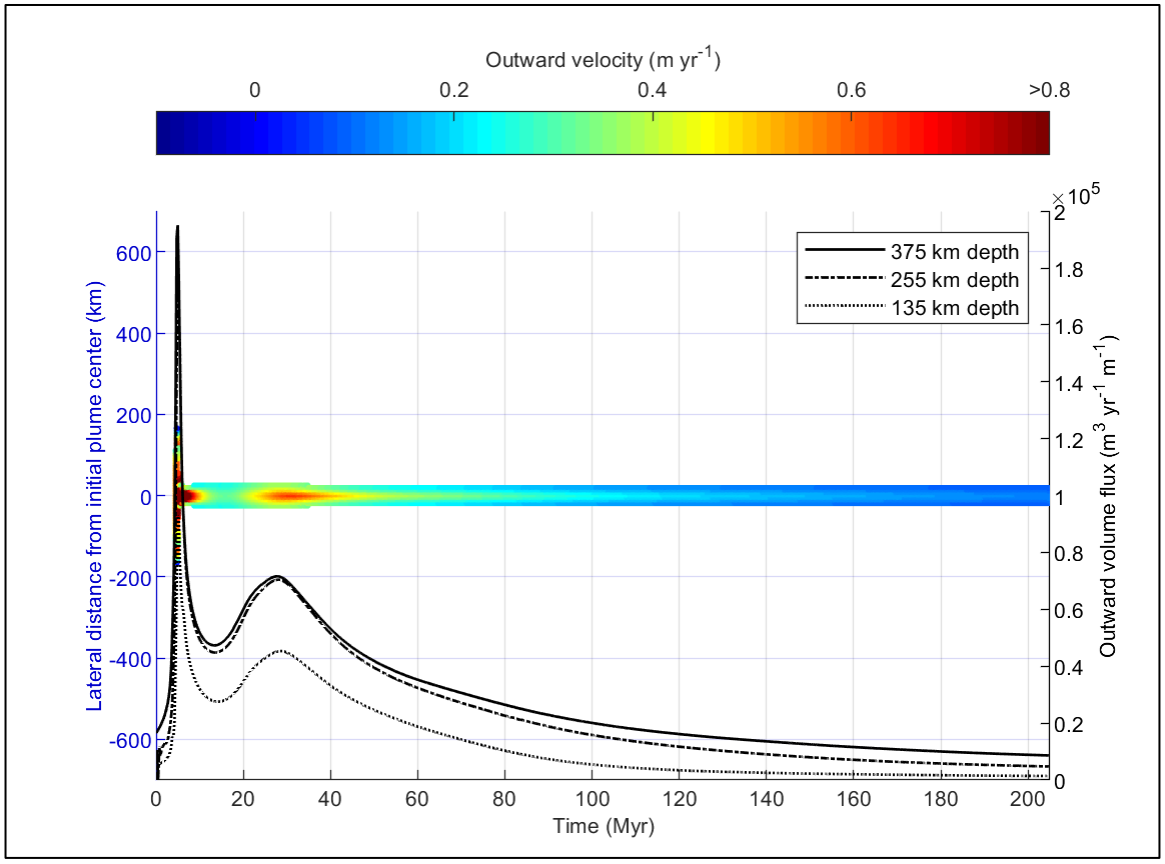

Figure 3.1 Comparison of outward volume flux (right axis), at depths of 375 km (solid line), 255 km (dashed line), and 135 km (dotted line), in a run with Clapeyron slopes of 0 MPa K^{-1} at the 410 km transition and -1 MPa K^{-1} at the 660 km transition. The left axis shows the plumes location relative to the model center (45º), with the colored points representing the plumes position and velocity over time.

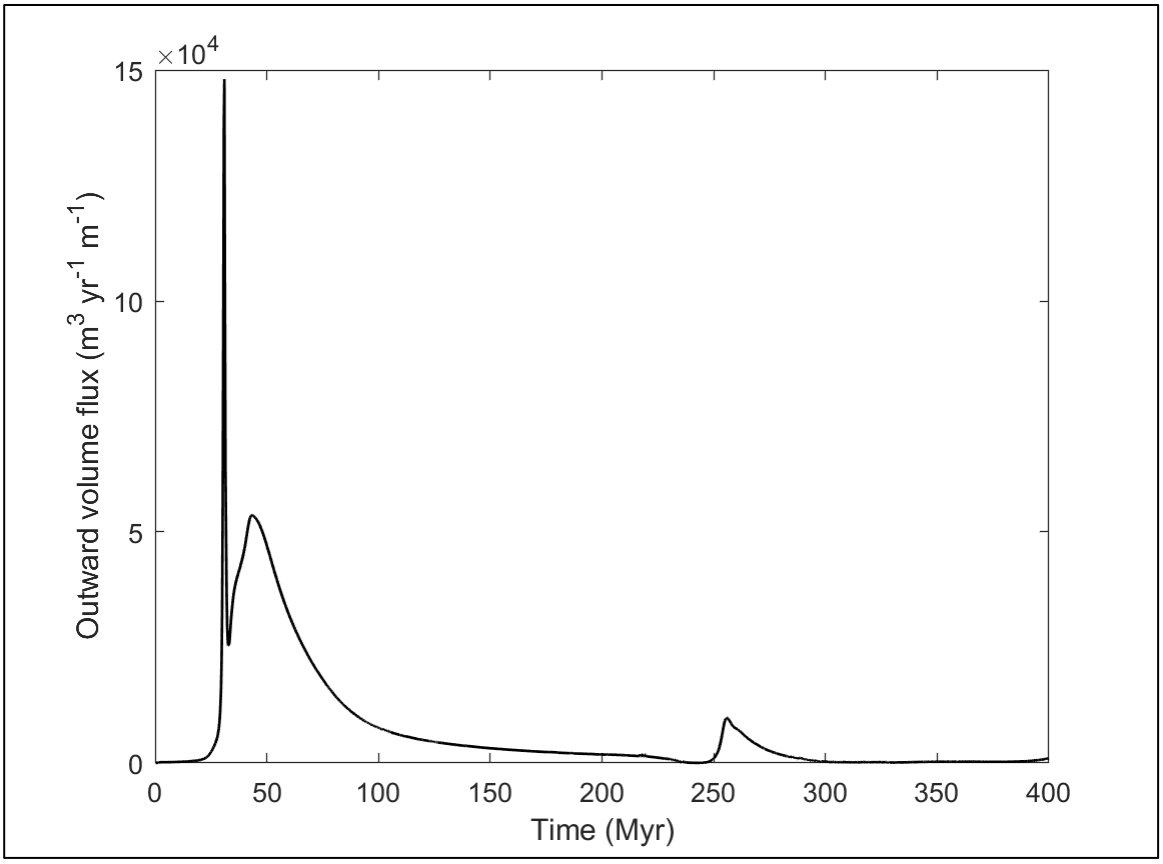

Figure 3.2 Outward volume flux across a depth of 375 km for a case with no plate motion, viscosity jump, or phase transitions.

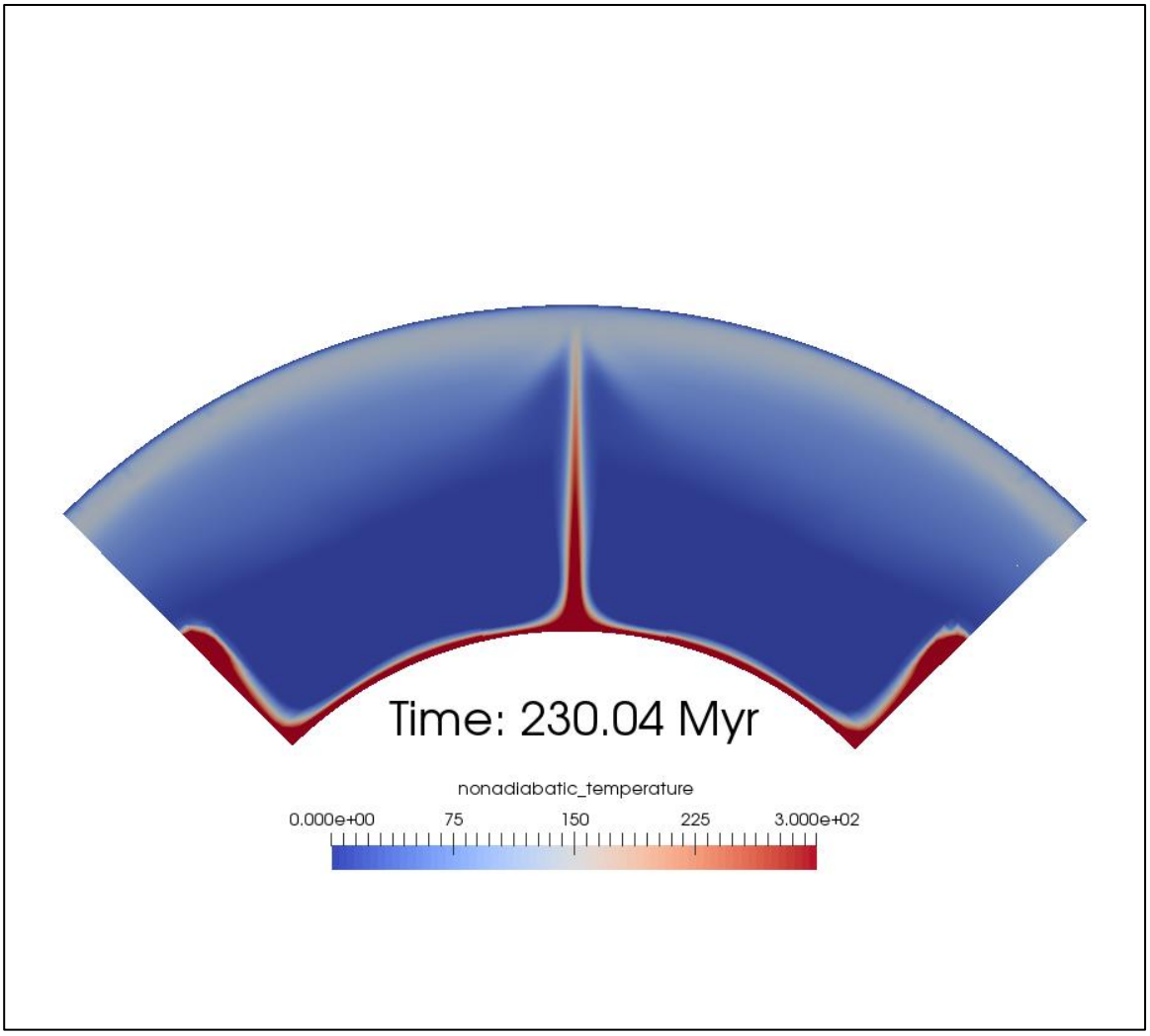

Figure 3.3 Secondary plumes initiating from the TBL at the model boundaries of a run with no plate motion, viscosity jump at 660 km, or phase transitions. Coloring represents the non-adiabatic temperature, or ΔT, of the run.

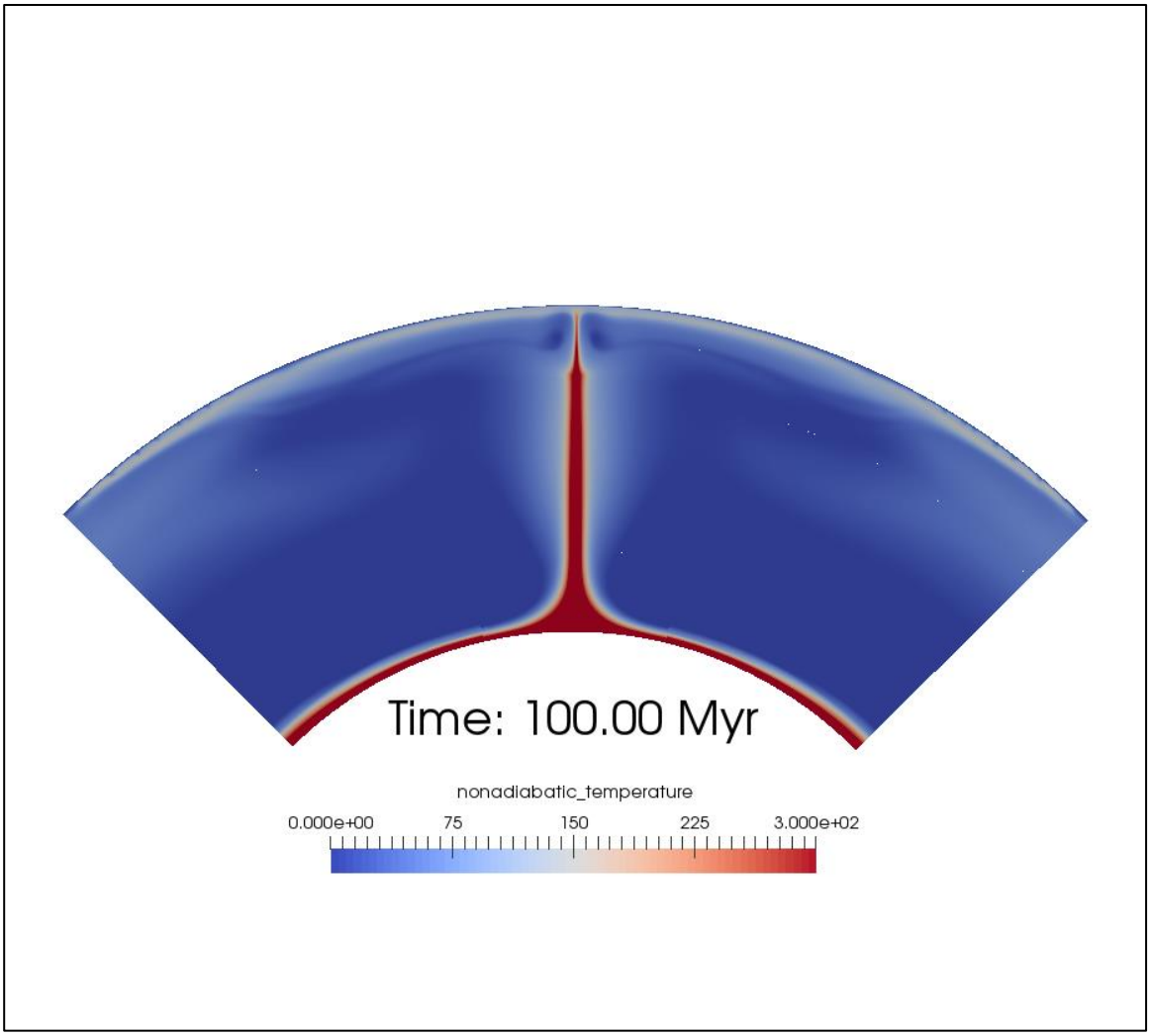

Figure 3.4 Adding a ~30x viscosity jump at 660 km depth results in a sharp decrease in plume conduit radius as it enters the much less viscous upper mantle. Coloring represents the non-adiabatic temperature of the plume and surrounding mantle.

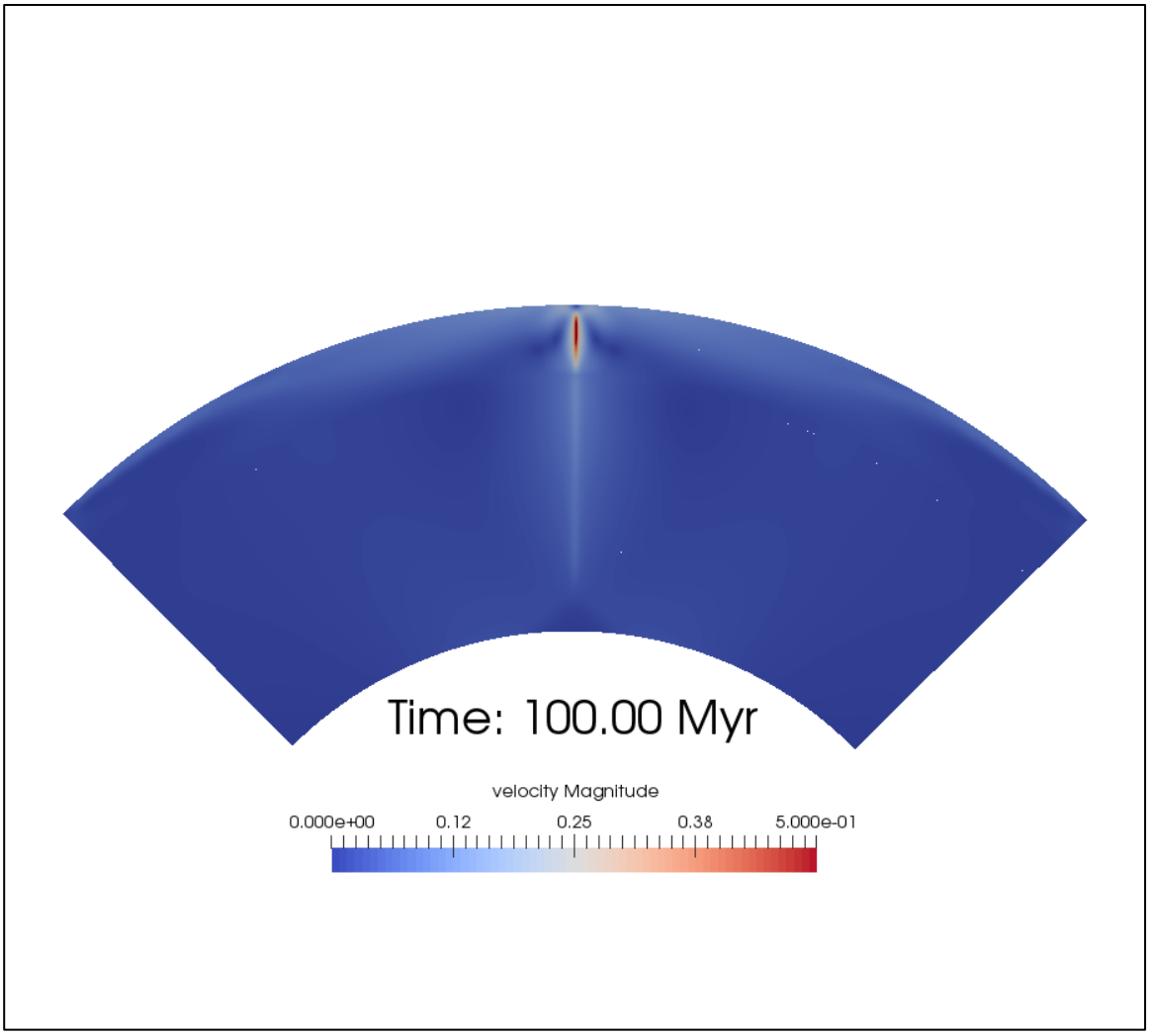

Figure 3.5 With an added viscosity jump (~30x) at 660 km depth, the plume conduit decreases in radius in the upper mantle. This results in higher velocities as the plume material is forced into the narrower conduit. Coloring represents the velocity, with the highest velocities in the upper mantle plume conduit.

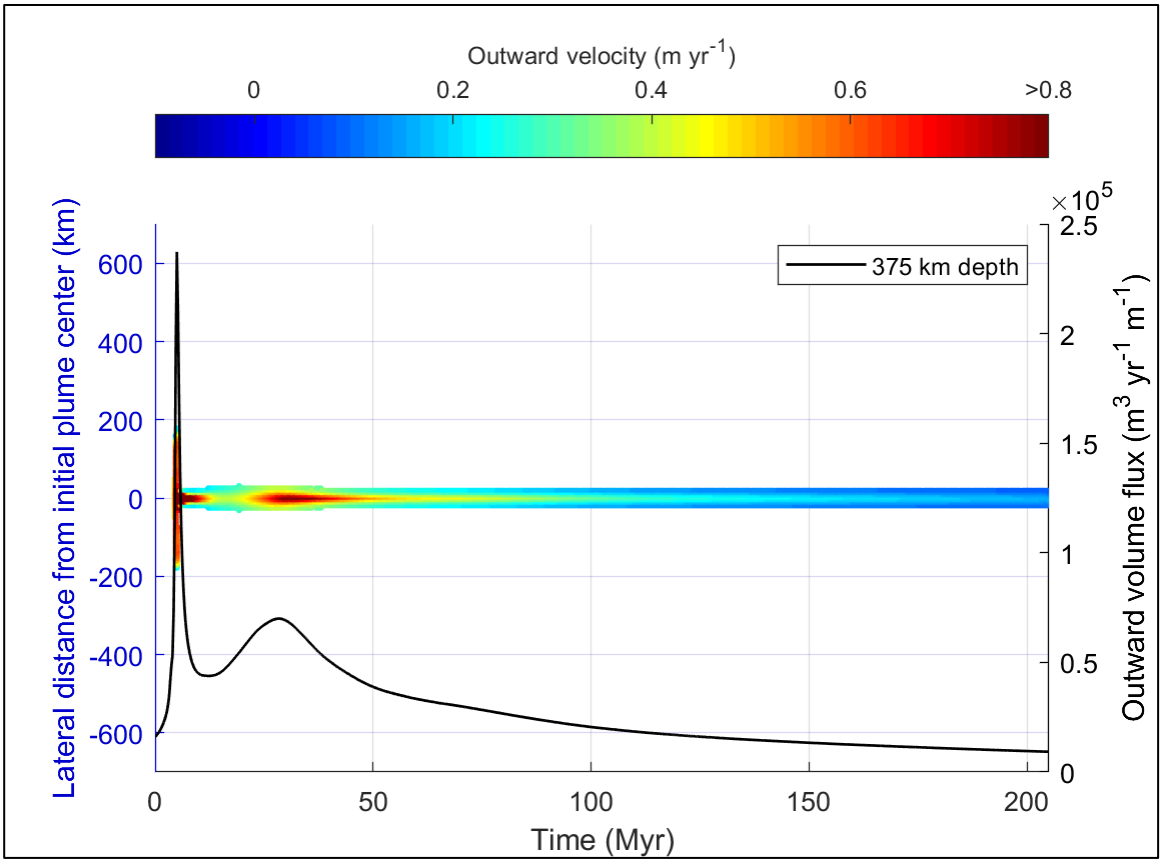

Figure 3.6 Outward volume flux (right axis) at 375 km depth in a run with no 410 km transition and a Clapeyron slope of -2 MPa K^{-1} at the 660 km transition. The left axis shows the plumes location relative to the model center (45º), with the colored points representing the plumes position and velocity over time. Figure shows a wider initial plume diameter and increase in volume flux at 5 Myr associated with the plume head. A second pulse later appears with an increase in velocity as the delayed plume stem reaches the upper mantle.

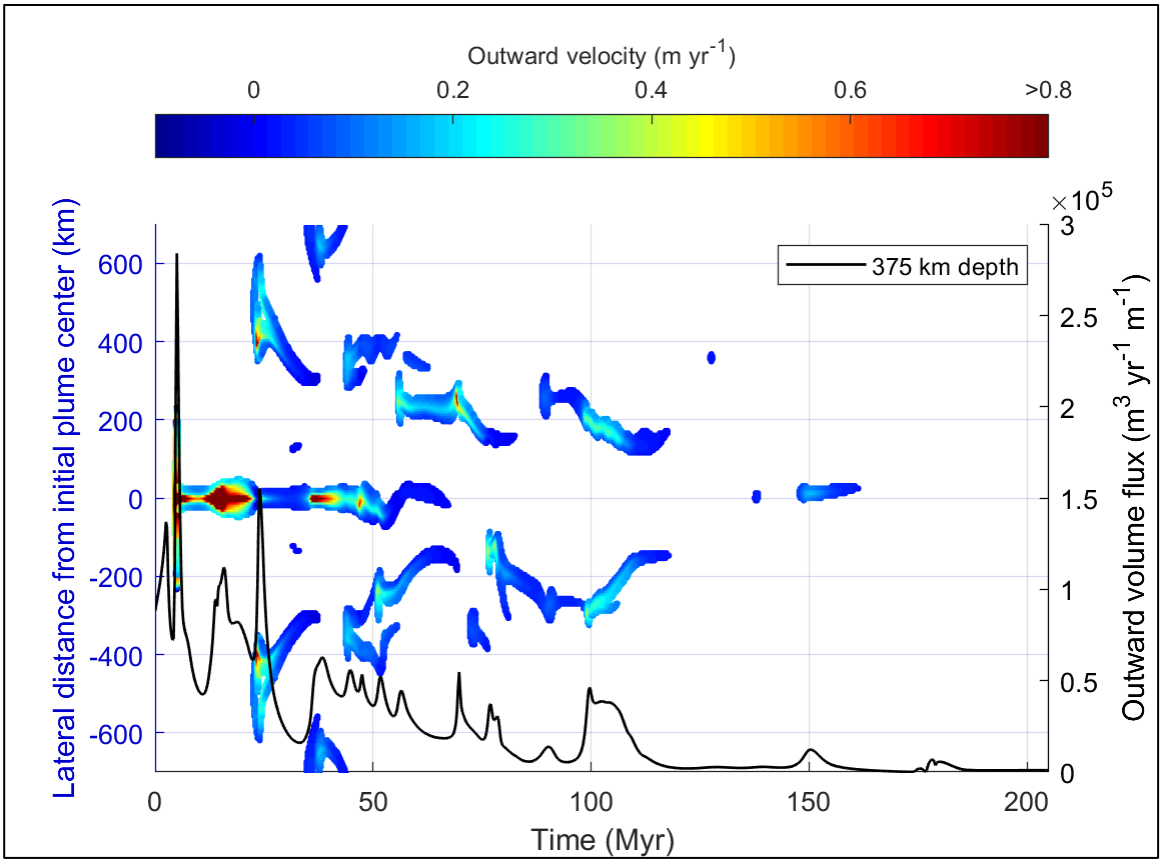

Figure 3.7 Outward volume flux (right axis) at 375 km depth in a run with no 410 km transition and a Clapeyron slope of -4 MPa K^{-1} at the 660 km transition. The left axis shows the plumes location relative to the model center (45º), with the colored points representing the plumes position and velocity over time. Figure illustrates the symmetrical formation of secondary plumes, that form closer to the center later in the model run.

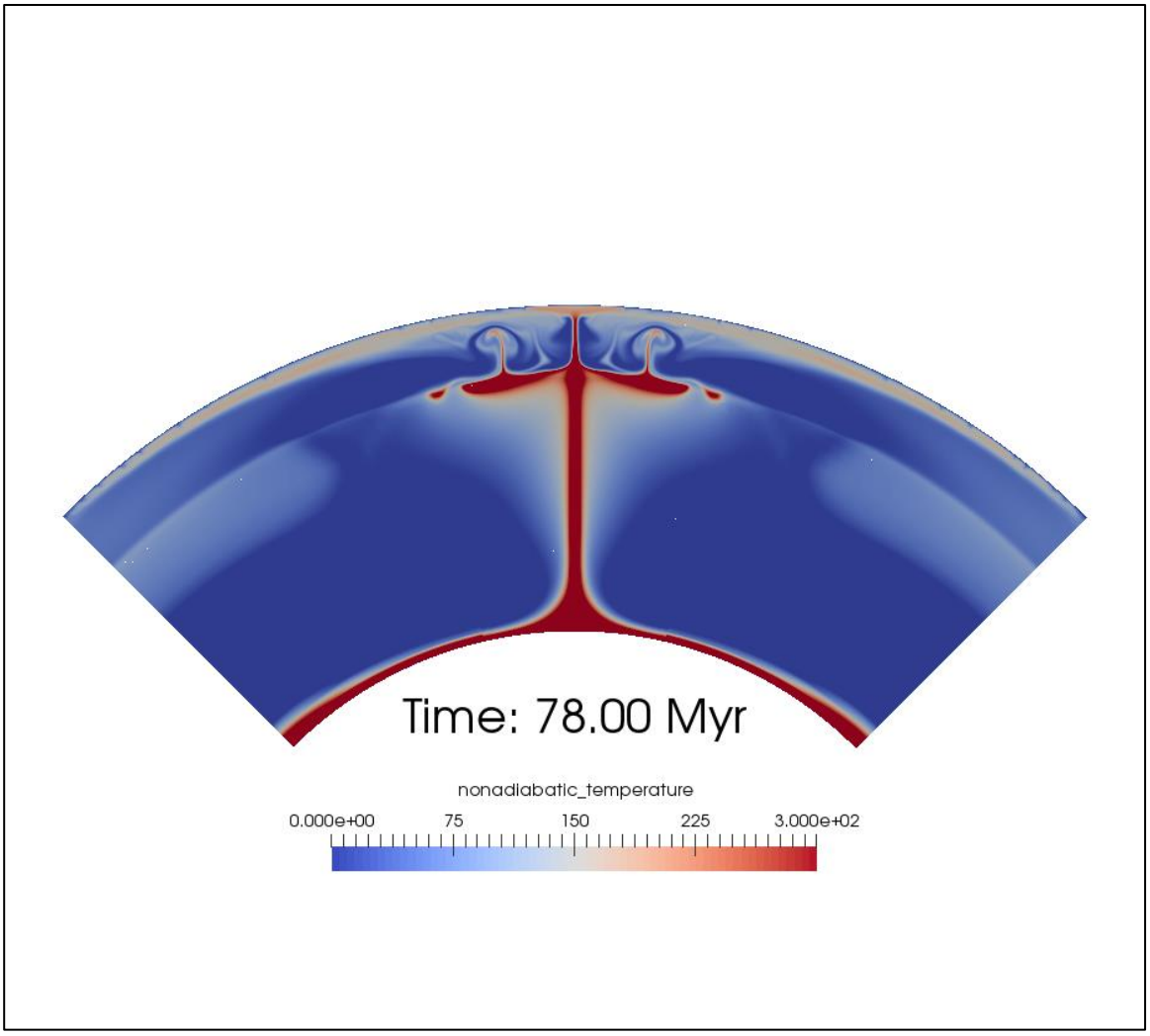

Figure 3.8 Image shows a run with no 410 km transition and a Clapeyron slope of -4 MPa K^{-1} at the 660 km transition. This leads to plume material ponding underneath the transition zone, forming a new TBL. Over time secondary plumes initiate from this TBL. Coloring represents the non-adiabatic temperature.

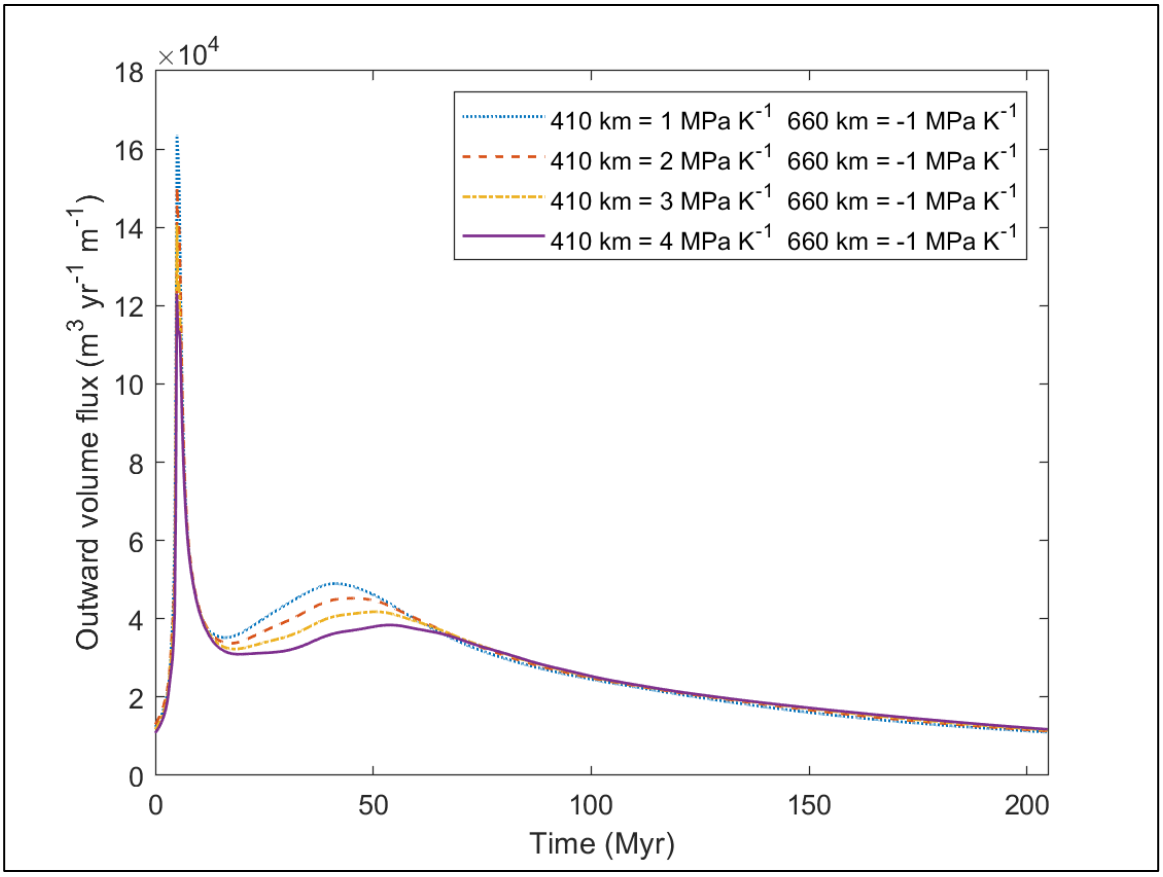

Figure 3.9 Volume flux comparison for runs with no plate motion, 410 km transition Clapeyron slopes of 1 MPa K^{-1} (dotted blue line), 2 MPa K^{-1} (dashed yellow line), 3 MPa K^{-1} (dashed red line) and 4 MPa K^{-1} (solid purple line), and a 660 km Clapeyon slope of -1 MPa K^{-1}. With increasing 410 Clapeyron slope, volume flux for the initial and secondary pulse lowers.

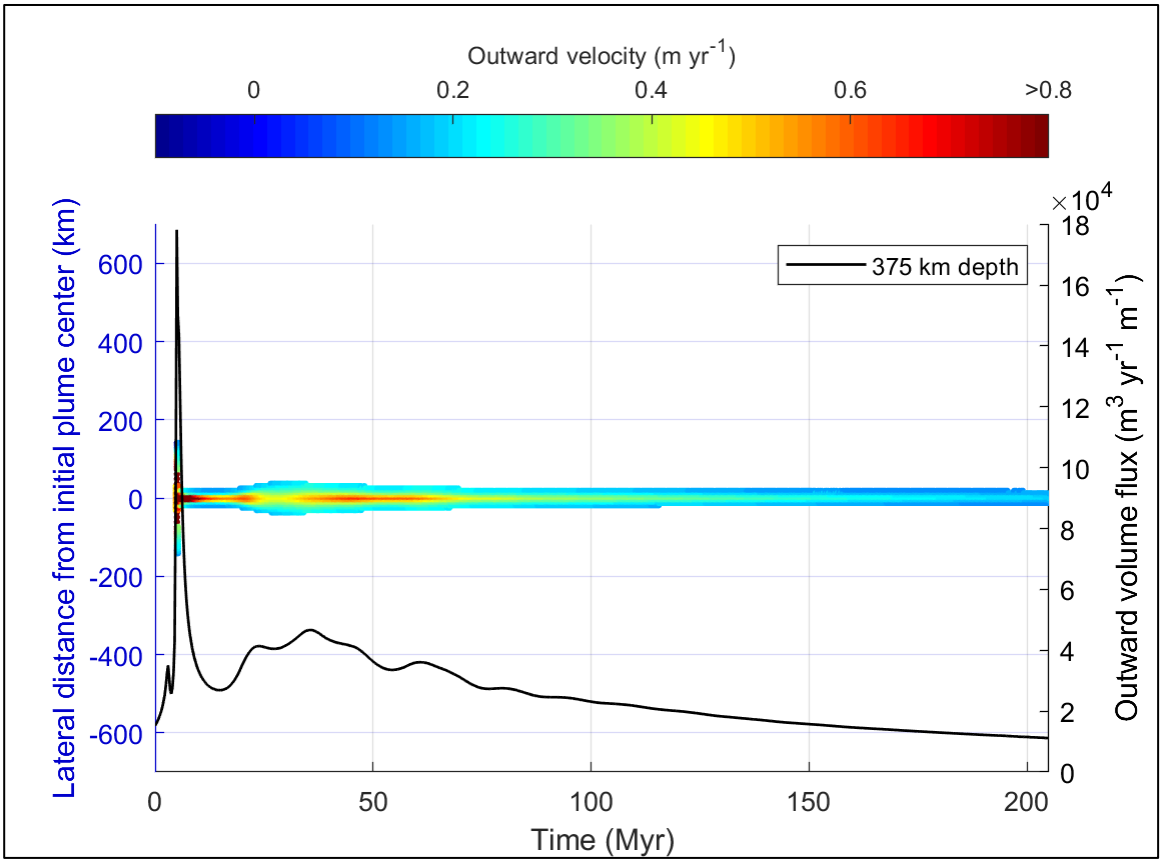

Figure 3.10 Outward volume flux (right axis) at 375 km depth in a run with Clapeyron slopes of 4 MPa K^{-1} at the 410 km transition and -3 MPa K^{-1} at the 660 km transition. The left axis shows the plumes location relative to the model center (45º), with the colored points representing the plumes position and velocity over time. As the 660 km Clapeyron slope nears a critical value (~-3.2 MPA K^{-1}) some variability appears in outward volume flux for ~80 Myr.

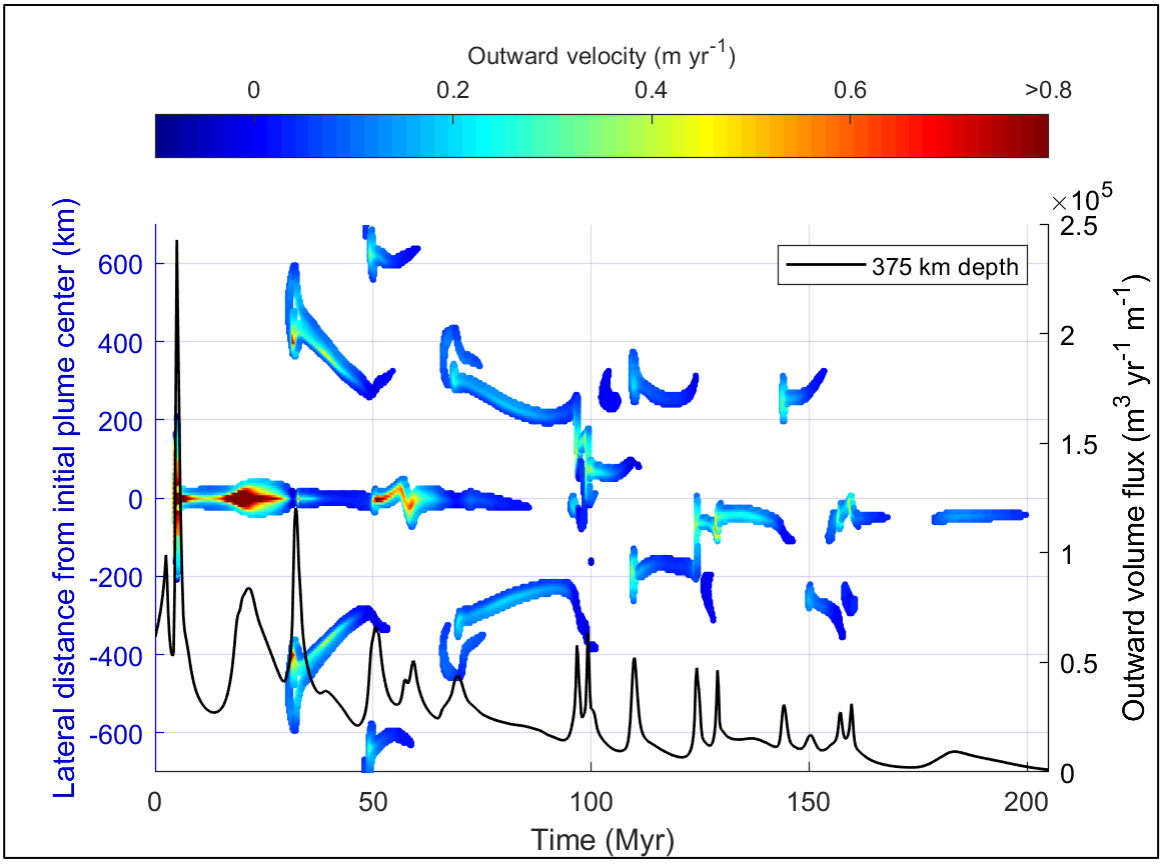

Figure 3.11 Outward volume flux (right axis) at 375 km depth in a run with Clapeyron slopes of 1 MPa K^{-1} at the 410 km transition and -4 MPa K^{-1} at the 660 km transition. The left axis shows the plumes location relative to the model center (45º), with the colored points representing the plumes position and velocity over time. With a lower 410 km transition Clapeyron slope, secondary plumes form symmetrically and often, forming closer to the center at later times.

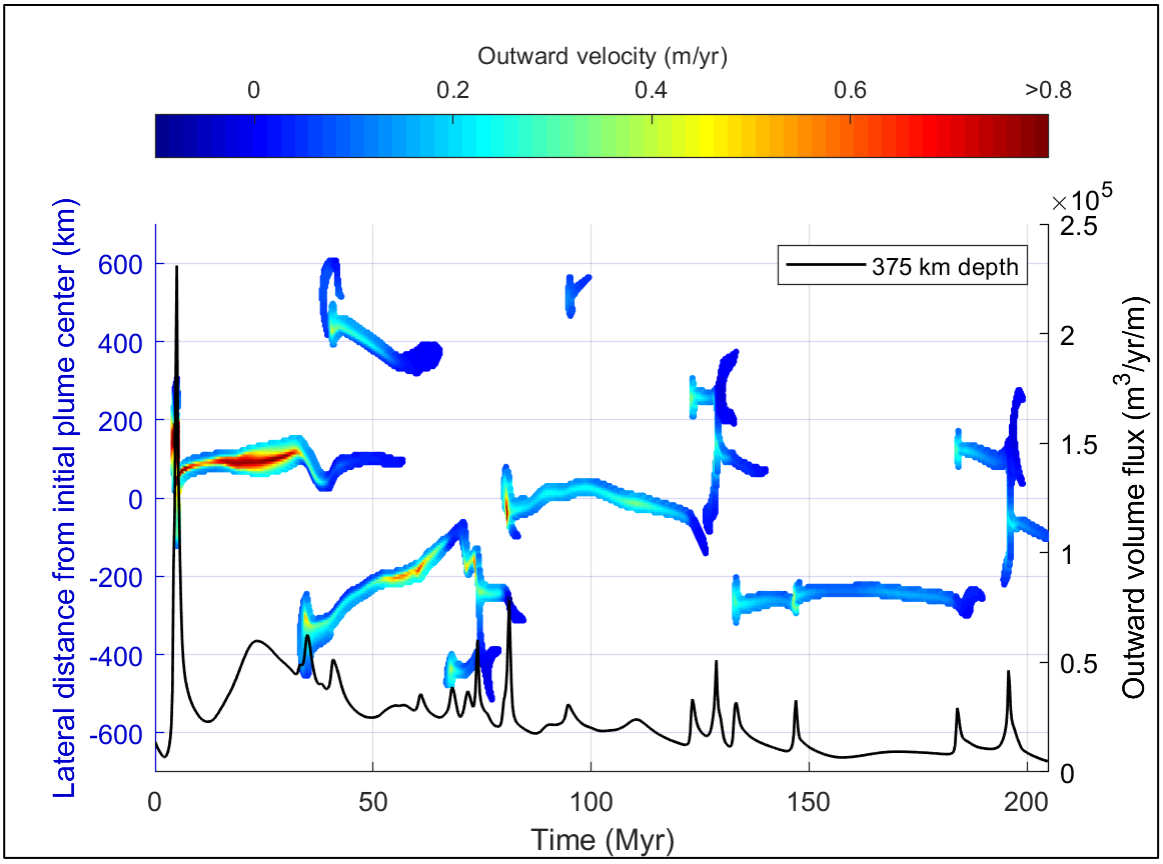

Figure 3.12 Outward volume flux (right axis) at 375 km depth in a run with Clapeyron slopes of 4 MPa K^{-1} at the 410 km transition and -4 MPa K^{-1} at the 660 km transition. The left axis shows the plumes location relative to the model center (45º), with the colored points representing the plumes position and velocity over time. With a higher 410 km transition Clapeyron slope we see fewer secondary plumes that are generally longer lasting.

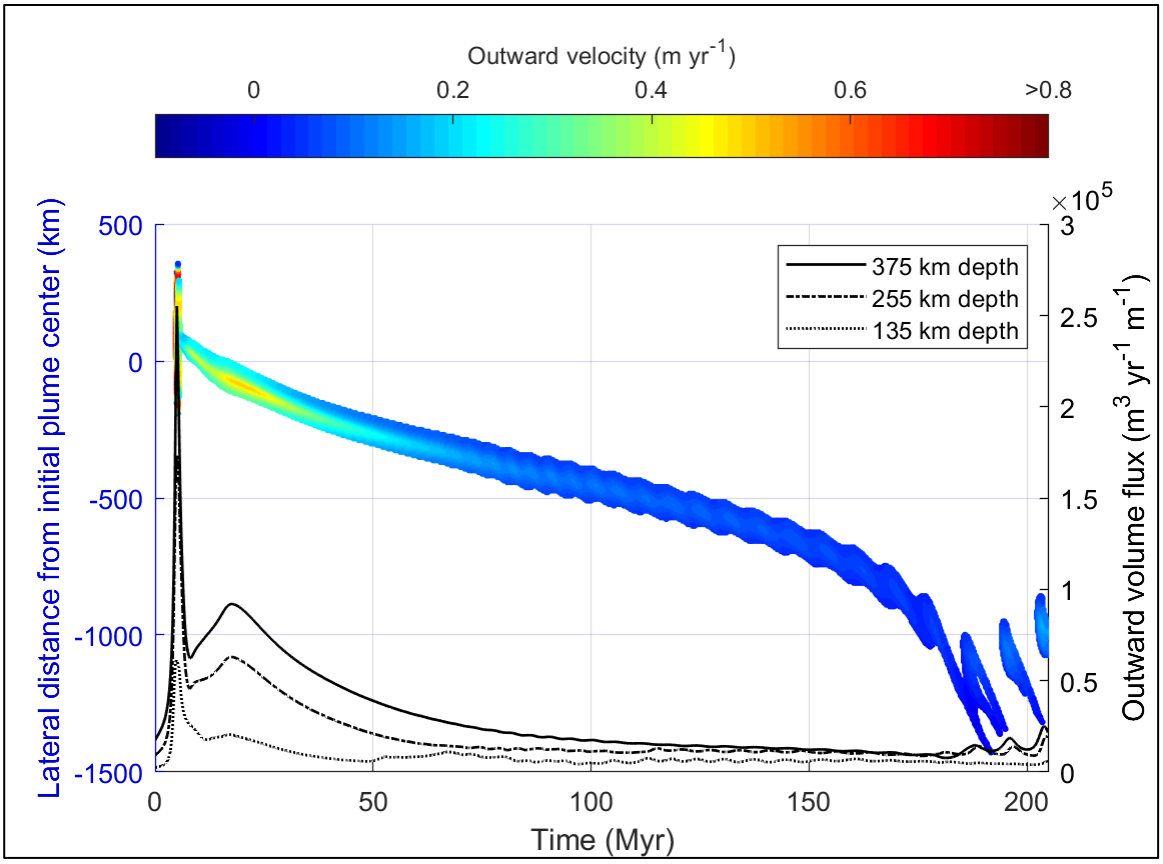

Figure 3.13 Outward volume flux comparison (right axis), at depths of 375 km (solid line), 255 km (dashed line), and 155 km (dotted line), in a run with no phase transitions or viscosity jump. Plate motion is set at 8 cm yr^{-1}. The left axis shows the plumes location relative to the model center (45º), with the colored points representing the plumes position and velocity over time.

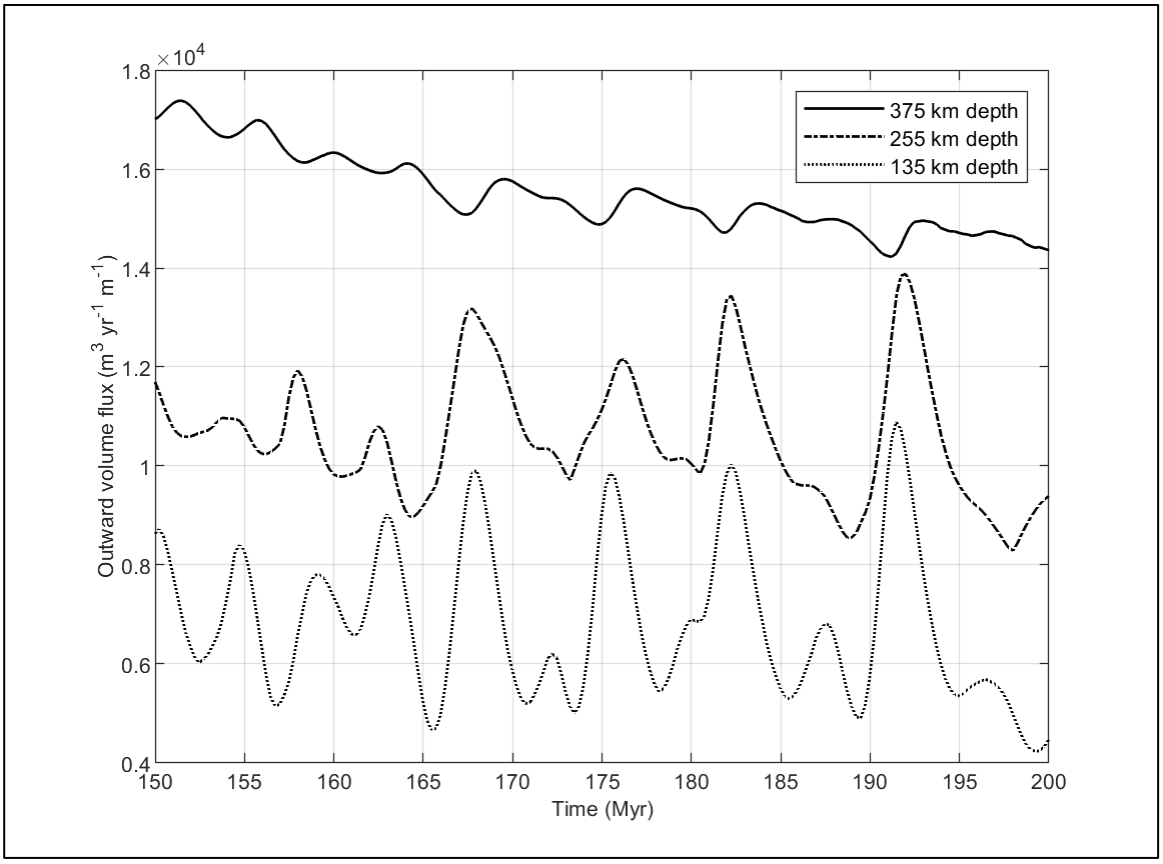

Figure 3.14 Outward volume flux variation appears at depths of 375 km (solid line), 255 km (dashed line), and 135 km (dotted line).

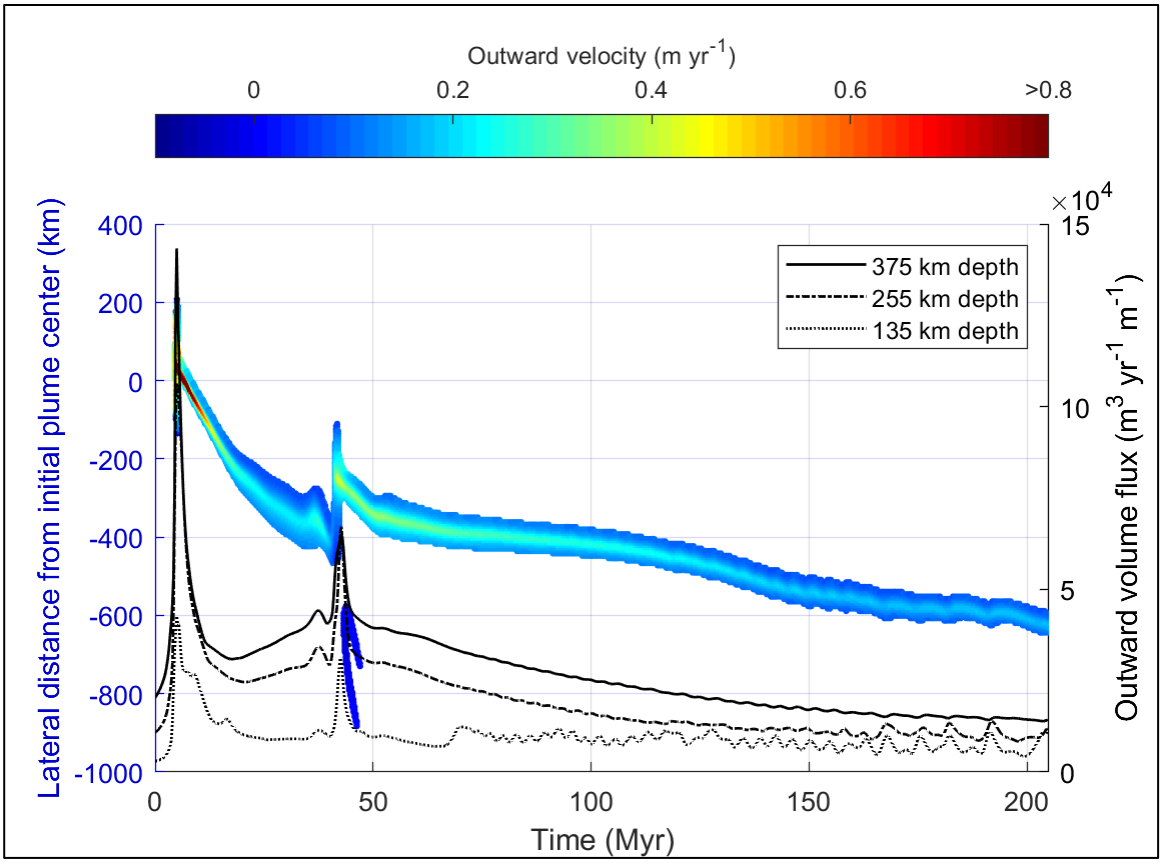

Figure 3.15 Outward volume flux comparison (right axis), at depths of 375 km (solid line), 255 km (dashed line), and 155 km (dotted line), in a run with Clapeyron slopes of 1 MPa K^{-1} at the 410 km transition and -1 MPa K^{-1} at the 660 km transition. Plate motion is set at 8 cm yr^{-1}. The left axis shows the plumes location relative to the model center (45º), with the colored points representing the plumes position and velocity over time. Figure shows one or two larger pulses from the 660 km transition (~45 Myr), and upper mantle pulsing begins ~70 Myr.

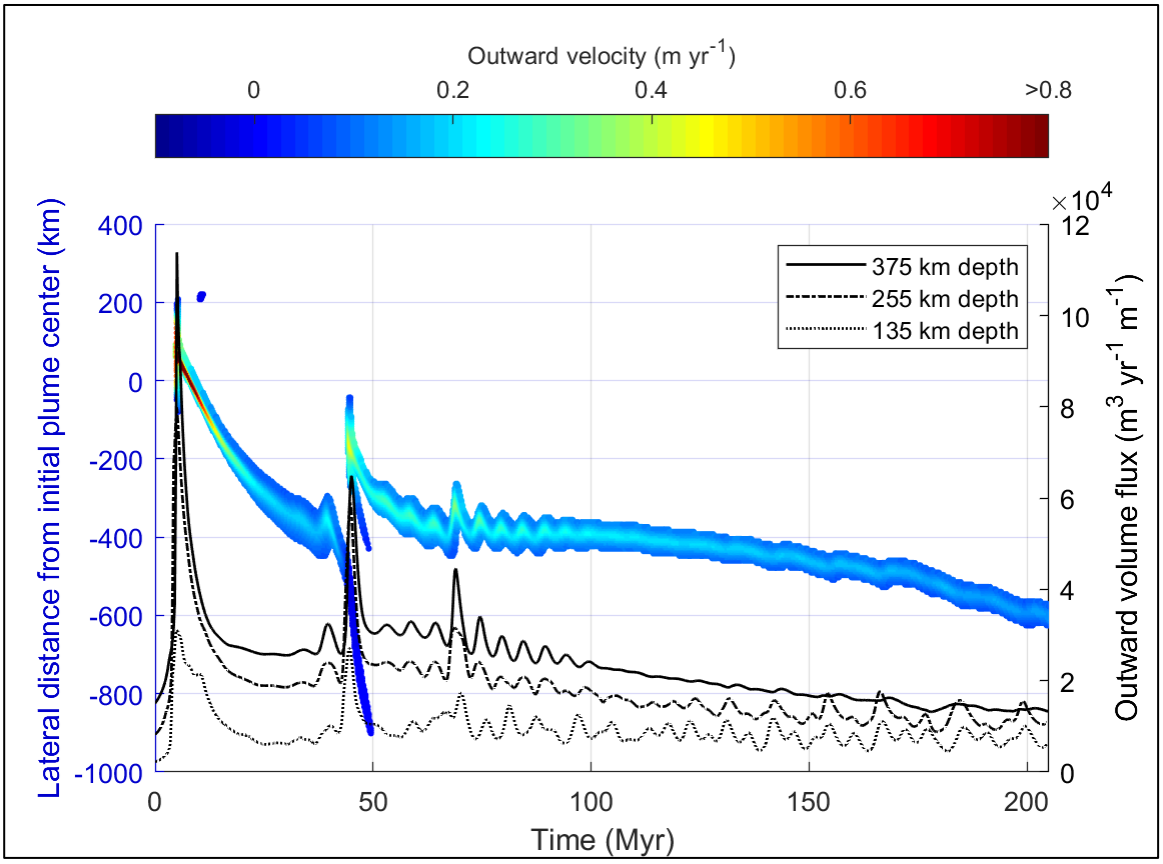

Figure 3.16 Outward volume flux comparison (right axis), at depths of 375 km (solid line), 255 km (dashed line), and 155 km (dotted line), in a run with Clapeyron slopes of 4 MPa K^{-1} at the 410 km transition and -1 MPa K^{-1} at the 660 km transition. Plate motion is set at 8 cm yr^{-1}. The left axis shows the plumes location relative to the model center (45º), with the colored points representing the plumes position and velocity over time. With a higher 410 km Clapeyron slope there is much more pulsing at the 660 km transition (~30-95 Myr).

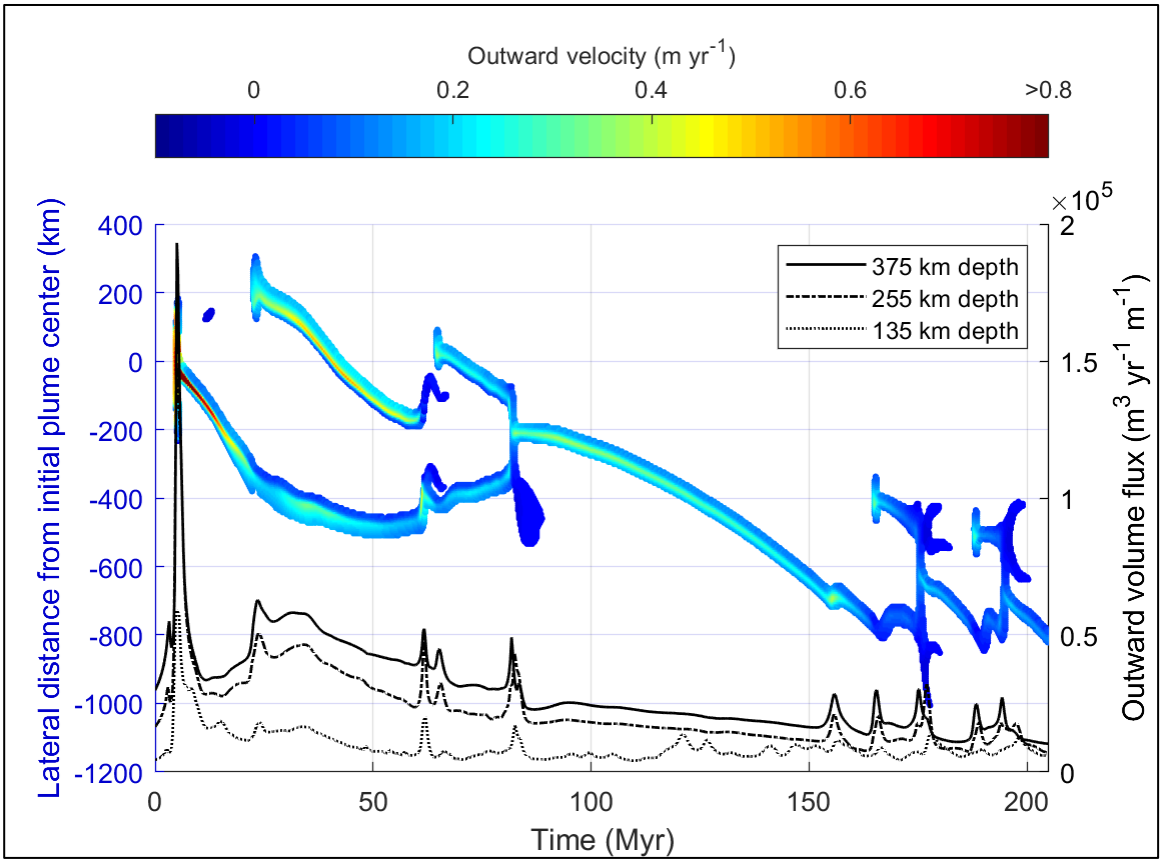

Figure 3.17 Outward volume flux comparison (right axis), at depths of 375 km (solid line), 255 km (dashed line), and 155 km (dotted line), in a run with Clapeyron slopes of 1 MPa K^{-1} at the 410 km transition and -3 MPa K^{-1} at the 660 km transition. Plate motion is set at 8 cm yr^{-1}. The left axis shows the plumes location relative to the model center (45º), with the colored points representing the plumes position and velocity over time.

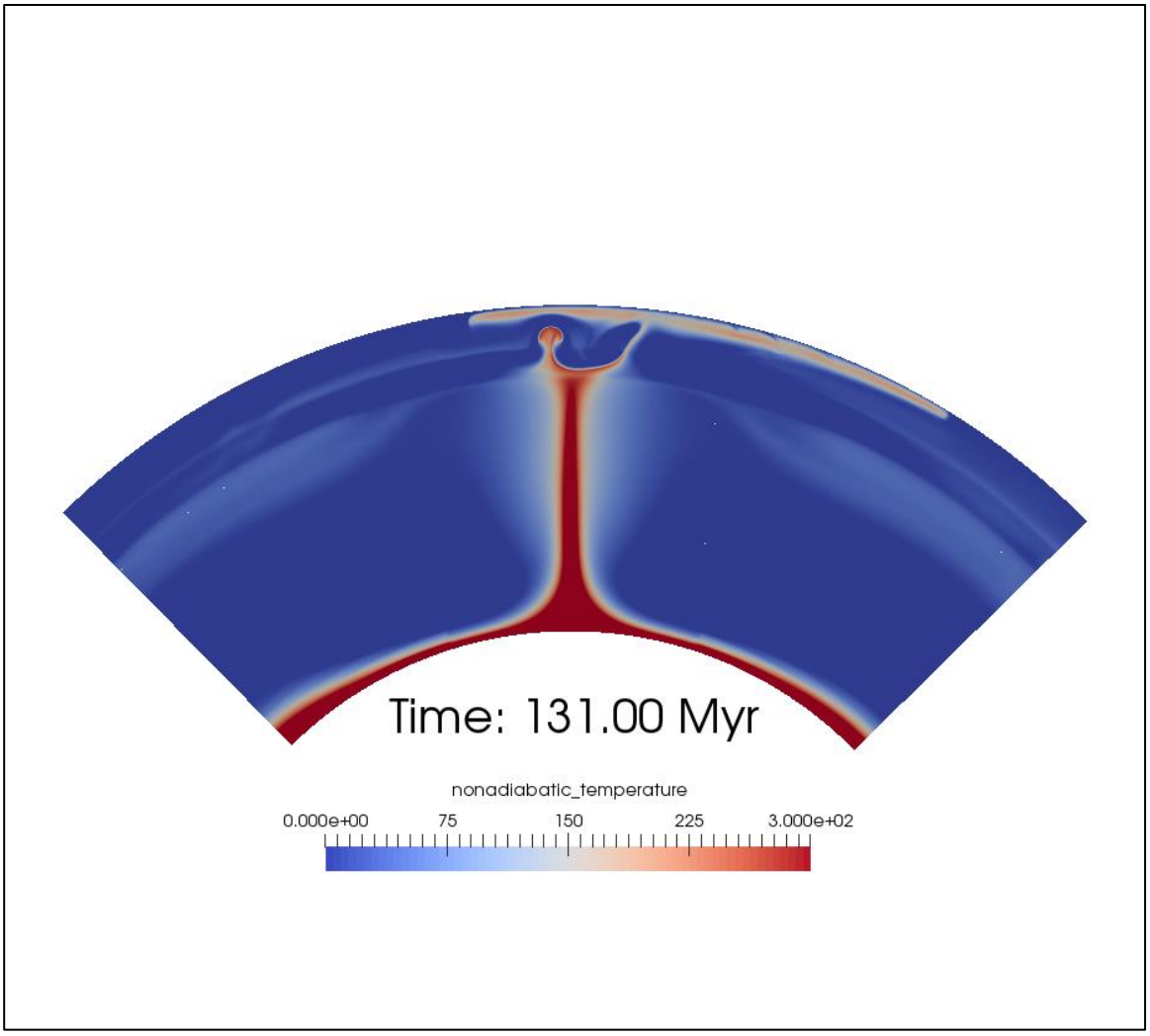

Figure 3.18 Formation of a secondary plume at the opposite edge of the mid-mantle TBL than the existing plume. Coloring represents non-adiabatic temperature.

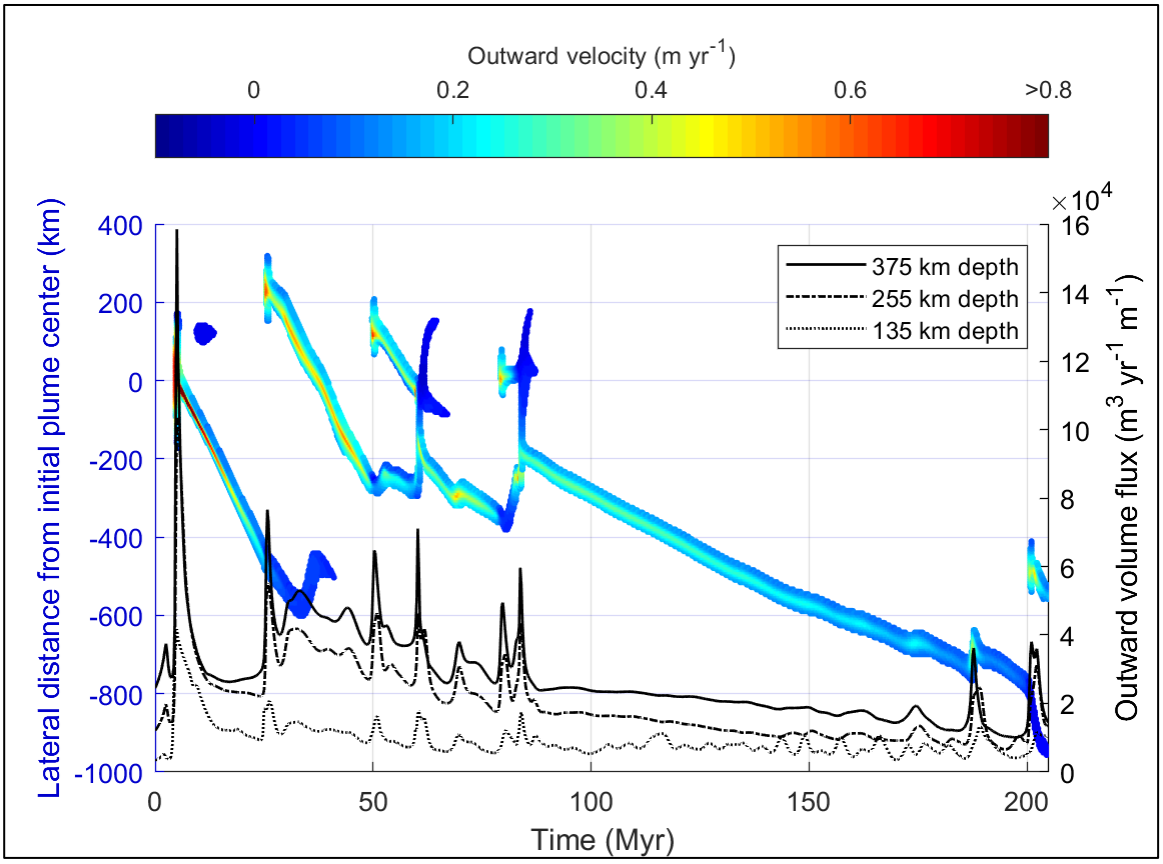

Figure 3.19 Outward volume flux comparison (right axis), at depths of 375 km (solid line), 255 km (dashed line), and 155 km (dotted line), in a run with Clapeyron slopes of 4 MPa K^{-1} at the 410 km transition and -3 MPa K^{-1} at the 660 km transition. Plate motion is set at 8 cm yr^{-1}. The left axis shows the plumes location relative to the model center (45º), with the colored points representing the plumes position and velocity over time.

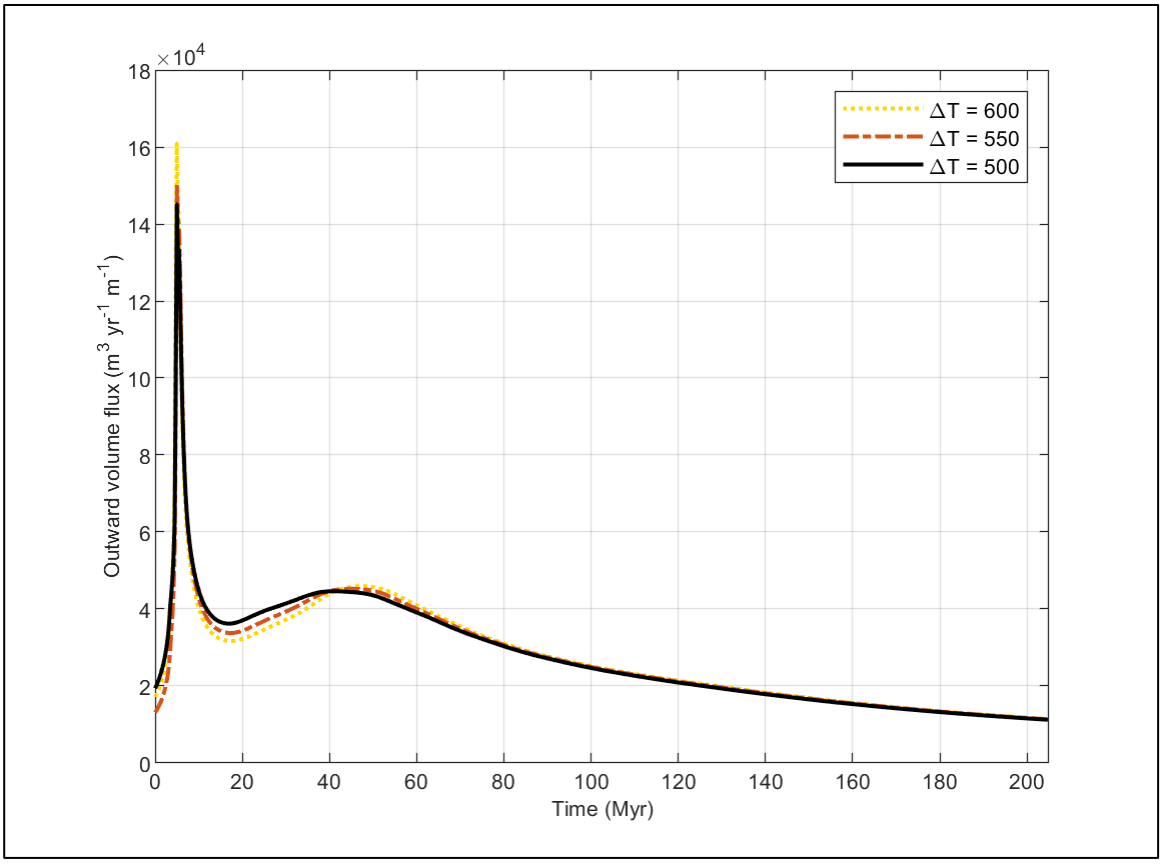

Figure 4.1 Outward volume flux comparison at 375 km depth of a run with Clapeyron slopes of 2 MPa K^{-1} at the 410 km transition and -1 MPa K^{-1} at the 660 km transition. Initial plume temperatures were 500 K (solid black line), 550 K (dashed red line), and 600 K (dotted yellow line).

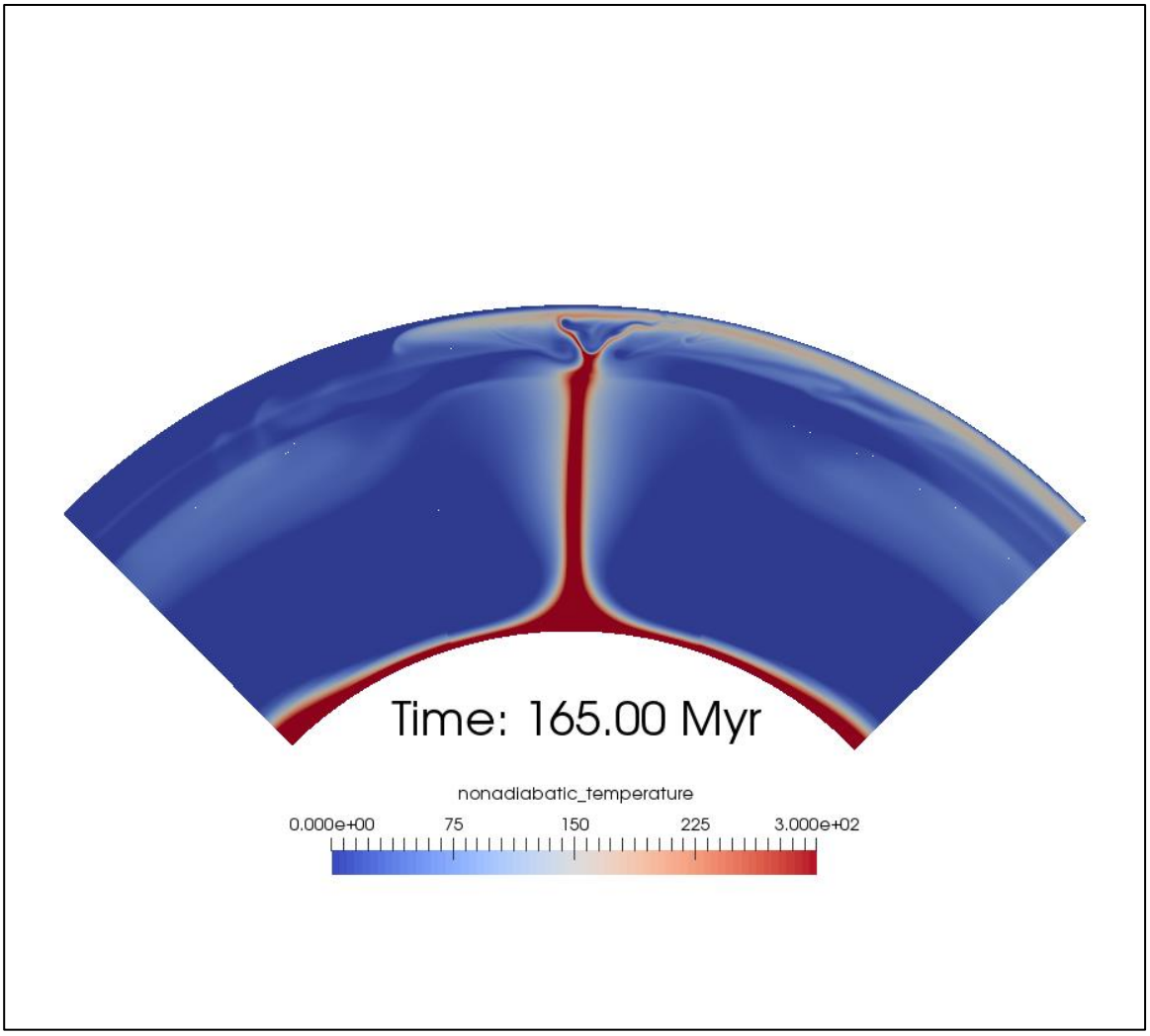

Figure 4.2 Plumes merging in transition zone, depth where they connect propagates upward over time.

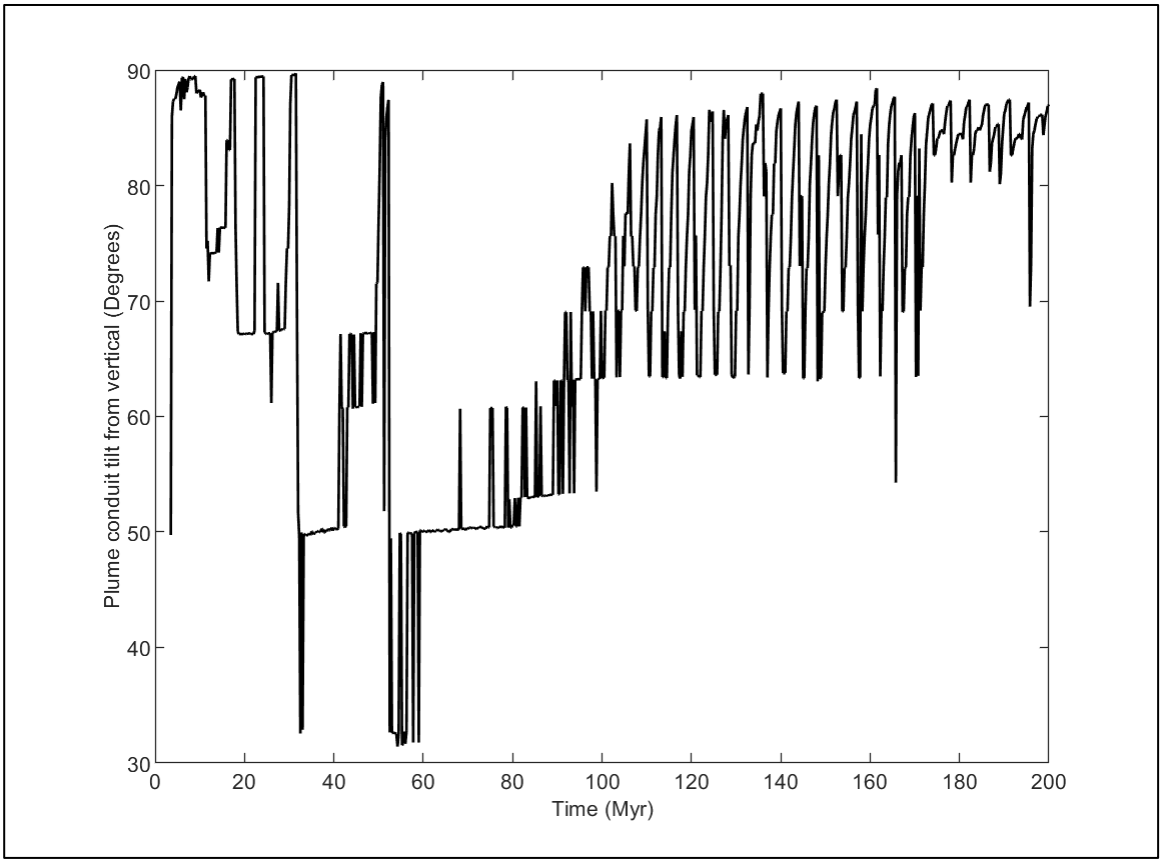

Figure 4.3 Tilt of the plume conduit from vertical from a run with Clapeyron slopes of 2 MPa K^{-1} at the 410 km transition and 2 MPa K^{-1} at the 660 km transition. Later in run with upper mantle pulsing (~93 Myr) tilt oscillates between ~63º and 88º

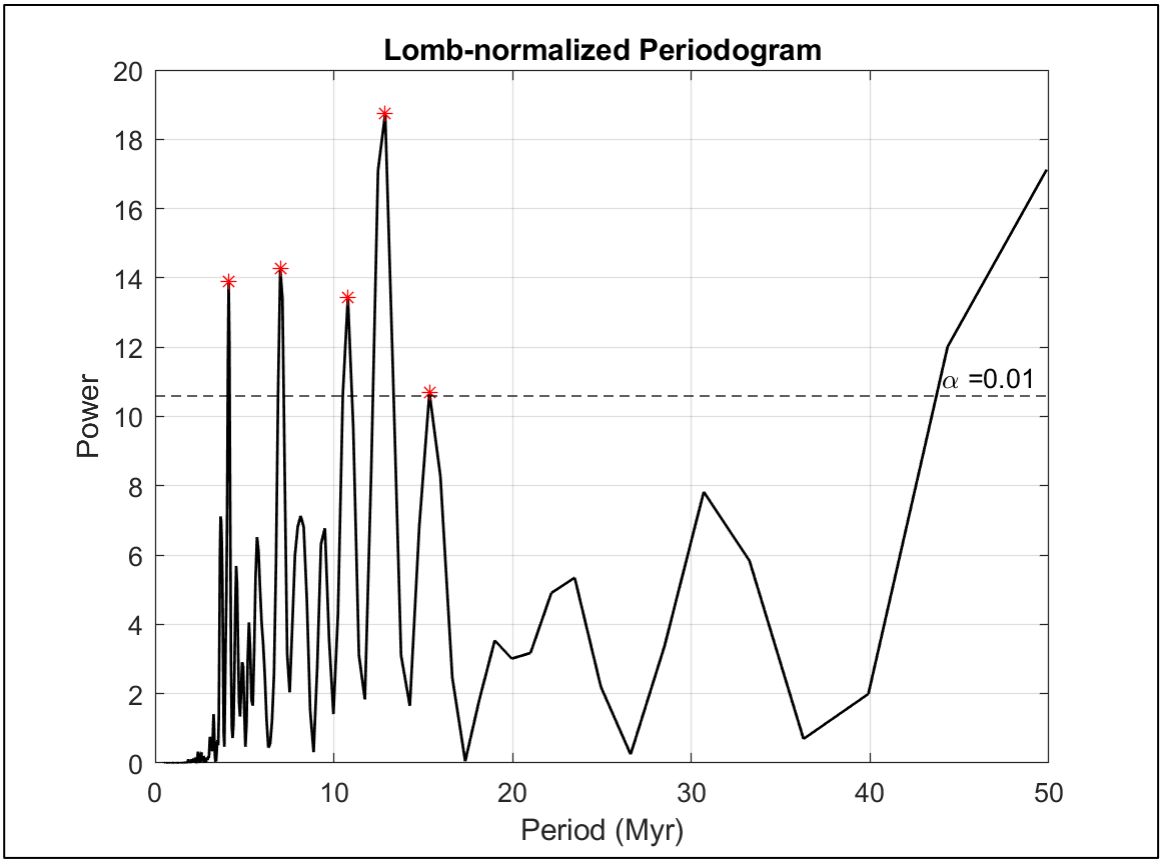

Figure 4.4 Periodogram of a run with Clapeyron slopes of 1 MPa K^{-1} at the 410 km transition and -1 MPa K^{-1} at the 660 km transition. The dashed line represents a significance ≥99%, peaks above this are sampled (red points)

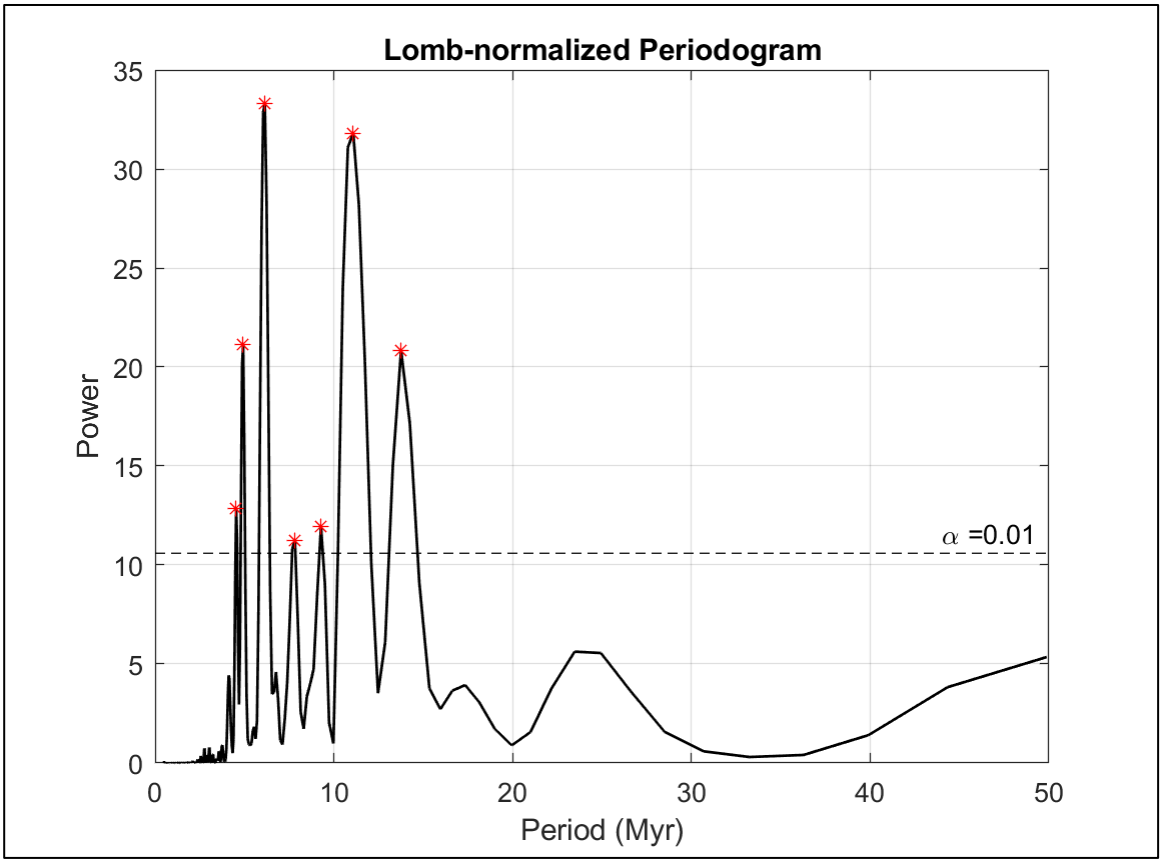

Figure 4.5 Periodogram of a run with Clapeyron slopes of 4 MPa K^{-1} at the 410 km transition and -1 MPa K^{-1} at the 660 km transition. The dashed line represents a significance ≥99%, peaks above this are sampled (red points)

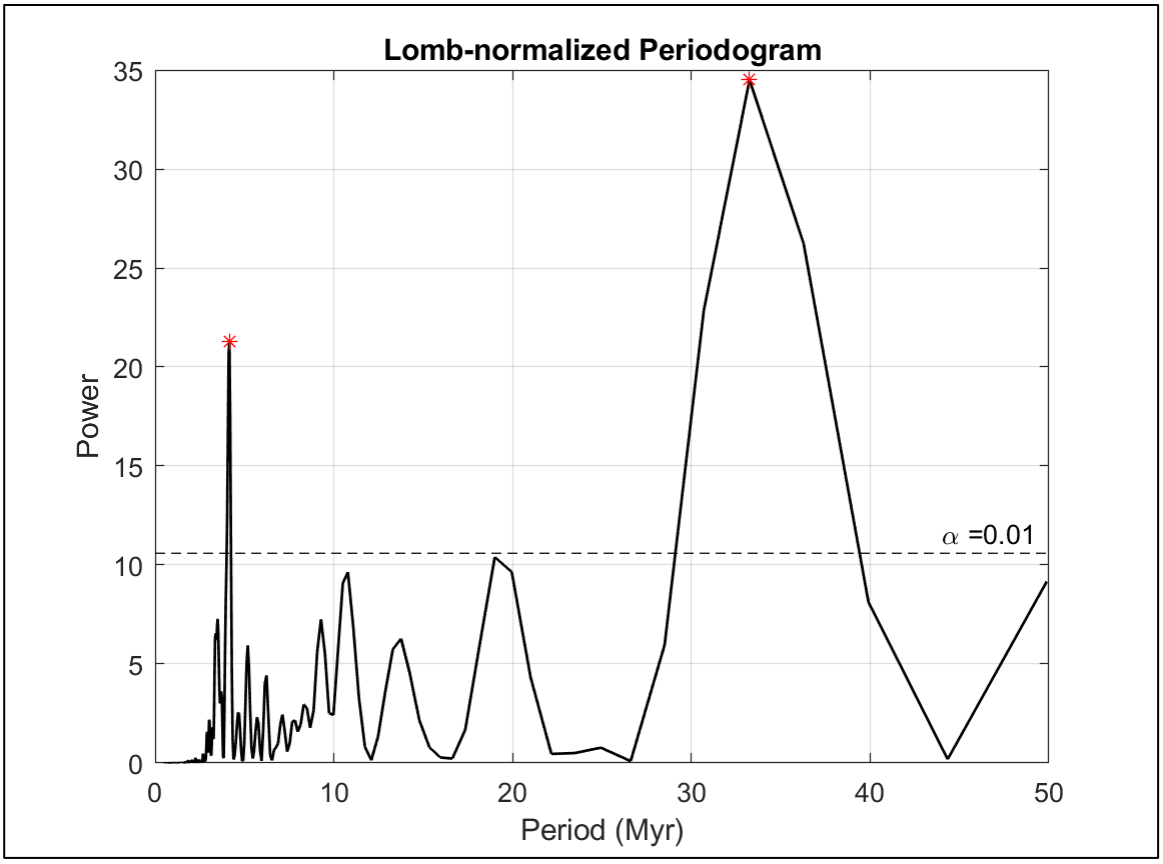

Figure 4.6 Periodogram of a run with Clapeyron slopes of 1 MPa K^{-1} at the 410 km transition and -2 MPa K^{-1} at the 660 km transition. The dashed line represents a significance ≥99%, peaks above this are sampled (red points)

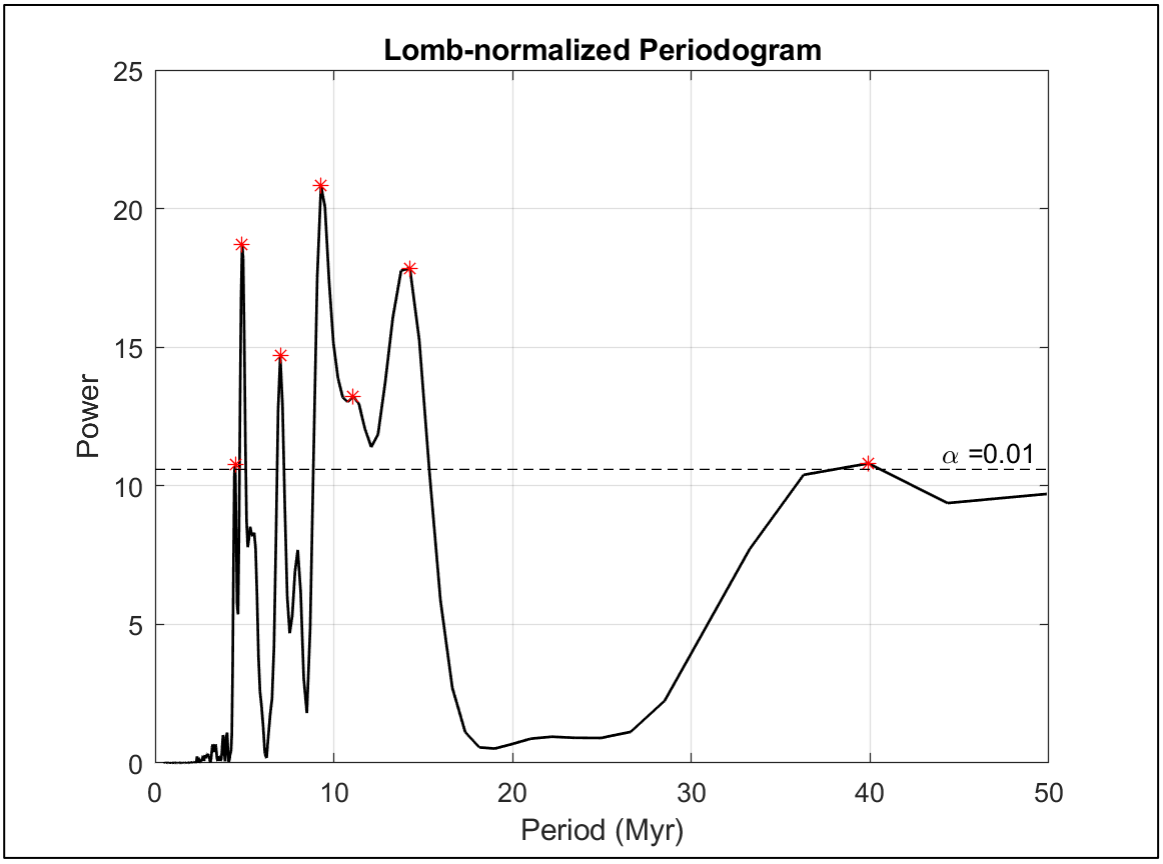

Figure 4.7 Periodogram of a run with Clapeyron slopes of 4 MPa K^{-1} at the 410 km transition and -1 MPa K^{-1} at the 660 km transition. The dashed line represents a significance ≥99%, peaks above this are sampled (red points)

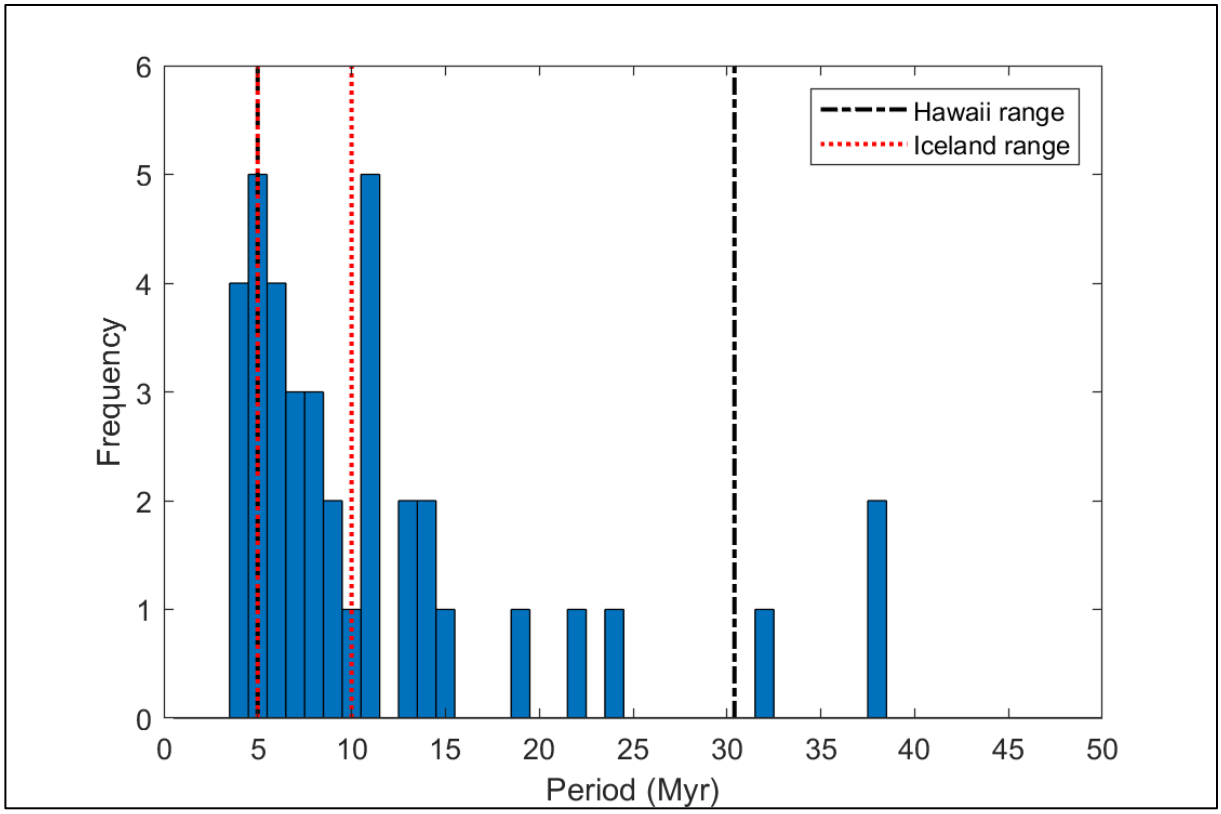

Figure 4.8 Histogram of periodicity peaks from upper mantle pulsing with a ≥99% significance for all 410 km transition Clapeyron slopes, and 660 km Clapeyron slopes. Red indicates periodicity range for Iceland, and black the periodicity range for Hawaii.

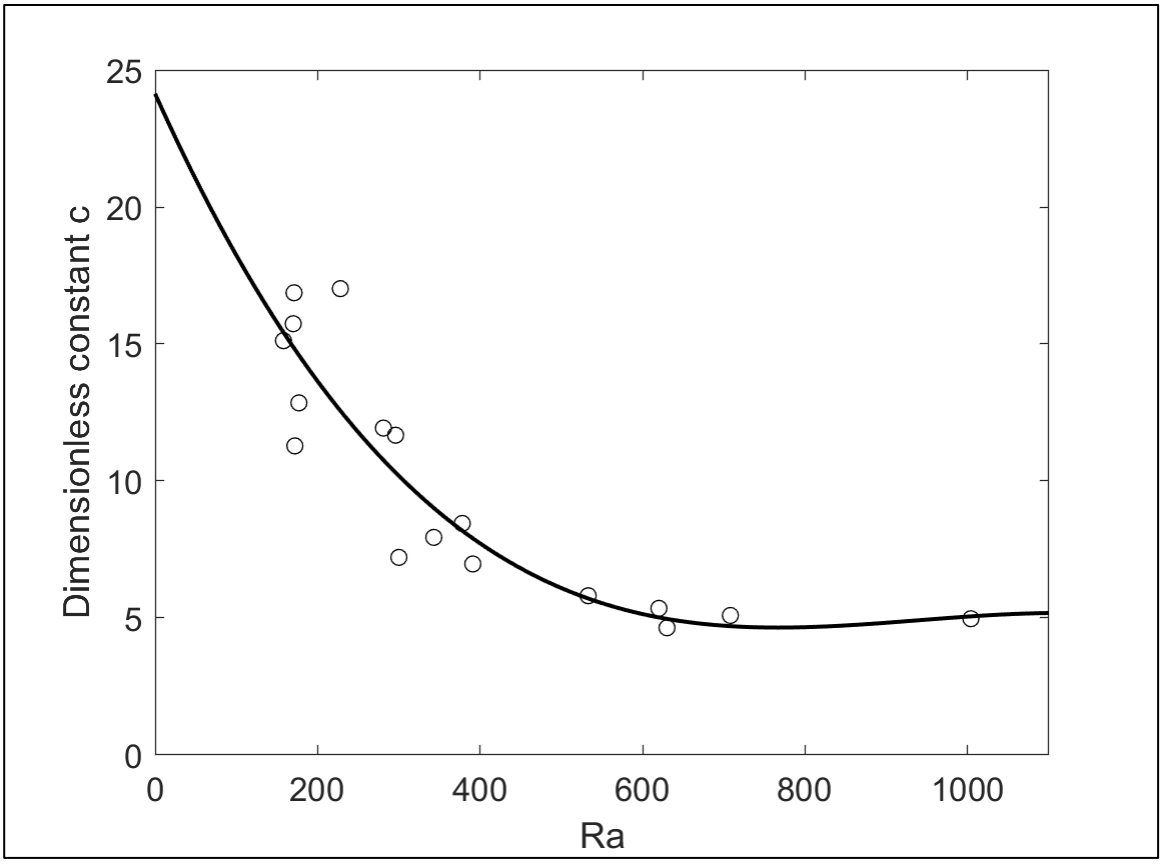

Figure 4.9 Third-degree polynomial fitted to experimental data (*Kerr et al*., 2008; *Meriaux et al*., 2011) to determine the corresponding dimensionless constant c value for a calculated plume Ra. C approaches 3.38 as Ra approaches infinity.

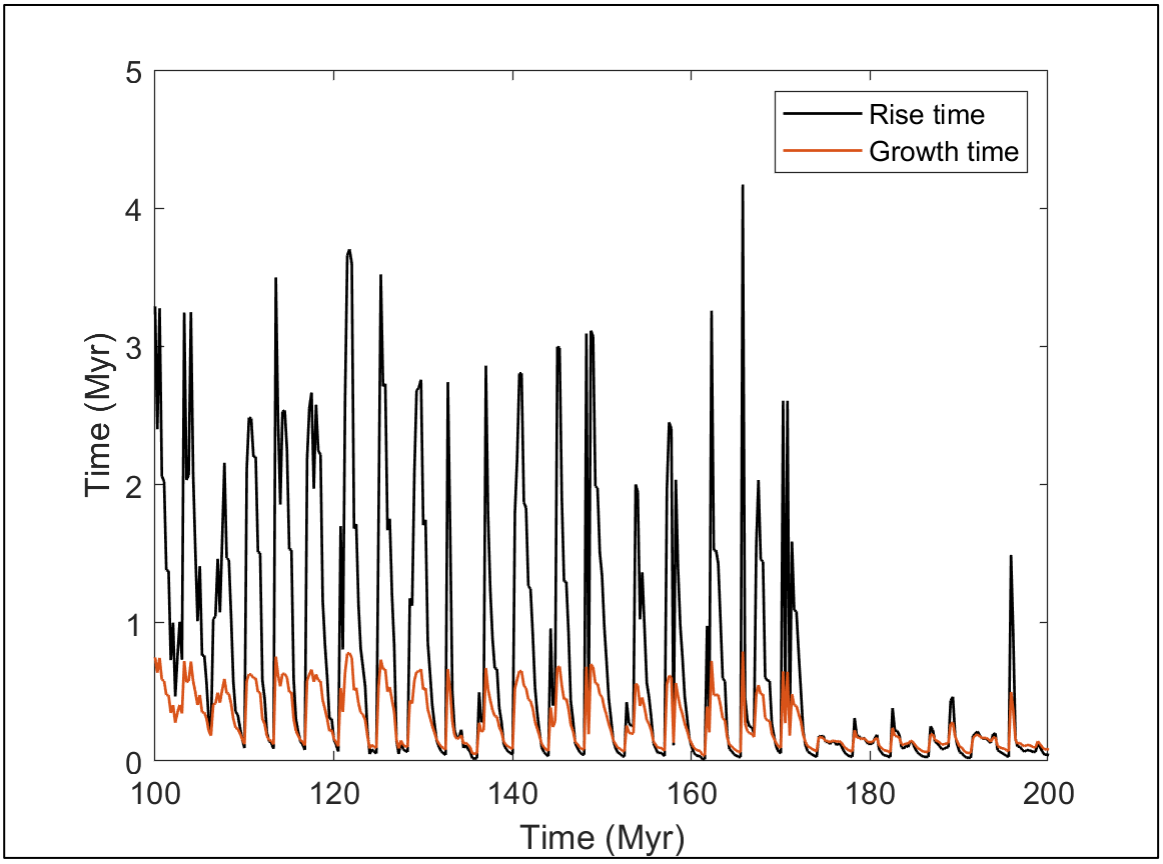

Figure 4.10 Comparison of the rise time (black line) and instability growth time (red line) of a plume conduit in a run with Clapeyron slopes of 2 MPa K^{-1} at the 410 km transition and -2 MPa K^{-1} at the 660 km transition.